July 1997

Interpreting the Thermal-Hydrological Response of the ESF Single Heater Test

Level 4 Milestone SP9267M4
Y.W. Tsang and J. T. Birkholzer
Earth Sciences Division, LBNL
1 Cyclotron Road, Mailstop: 90-1116
Berkeley CA 94720

1. Introduction

The Single Heater Test (SHT) is part of the Exploratory Studies Facility (ESF) Thermal Test being conducted underground at the potential high-level nuclear waste repository at Yucca Mountain, Nevada. The purpose of the ESF Thermal Test is to better understand the coupled thermal, mechanical, hydrological, and chemical processes likely to exist in the rock mass surrounding the potential geological repository at Yucca Mountain. These coupled processes are monitored by a multitude of sensors installed in the various instrumented boreholes to measure the temperature, humidity, gas pressure, mechanical displacement, and stresses of the rock mass in response to the heat generated in the single heater. On August 26, 1996, the 5-m-long heater in the Single Heater Test (SHT) was turned on, the heat was turned off on May 28, 1997, nine months later. A cooling period of nine months to a year is planned before the termination of the SHT. The complete set of data for the entire heating phase of the SHT has now been made available (Homuth, 1996-1997) to the thermal testing team.

As members of the thermal testing team, we have performed pretest predictive simulations of the anticipated rock mass thermal-hydrological response to the SHT (Birkholzer and Tsang, 1996). The objective of that study was to use the "best" input parameters and "most reasonable" conceptualization available, at the time of the predictive simulations, to create a baseline model. Thus the configuration, parameters, initial and boundary conditions of that numerical model are designed to resemble the actual Single Heater Test as closely as possible. Furthermore, all site-specific pre-heat characterization data, such as laboratory measurements of core thermal and hydrological properties from the SHT block, fracture mapping of the drifts in the Thermo-mechanical alcove, *in-situ* air permeability characterization (Tsang et al., 1996), and borehole video logs, are incorporated in the conceptual model for numerical simulations of the SHT. However, due to the complexity of the multiple physical processes, and uncertainty in key parameters such as fracture properties, as well as the spatial variability of formation properties in the SHT block, it was fully recognized at the time of that report's preparation (Birkholzer and Tsang, 1996) that the simulated results from any one numerical model will deviate from actual data. Therefore, a number of sensitivity studies were presented in that report to help understand

how individual processes and input parameters affect the thermal-hydrological performance, and to provide insight to plausible causes of discrepancy between simulations and real data as they become available.

This report seeks to provide interpretation of the measured data, based on the understanding gained in the simulations and sensitivity studies ca ried out for the thermal-hydrological baseline model. The measured data from the SHT (from the onset of heating through May 31, 1997) will be compared to SHT heating phase predictions by the baseline model presented in Birkholzer and Tsang (1996). Where a discrepancy between predication and measurement occurs, the possible causes will be discussed, and additional simulations will be presented in this report to refine and calibrate the baseline model. These additional simulations may also incorporate new information not available at the time of the earlier report.

2. Thermal Hydrological Data

The most prominent rock mass thermal-hydrological response of the SHT to the heater power output is the boiling of water from the temperature rise and the initial drying of the rock mass surrounding the heater, the carrying away of moisture in the form of vapor from the heated area, and the subsequent condensation of the vapor in the cooler regions of the rock mass, farther away from the single heater. As the power output of the single heater is turned off during the cooling phase, rewetting occurs as water moves back to the vicinity of the heater under the driving force of capillary suction. The vaporization, drying, condensation, and rewetting processes are reflected in the spatial variation and temporal evolution of the moisture content in the rock mass. In light of this, the measured quantities that monitor the thermal-hydrological response of the SHT are temperature, gas pressure, and relative humidity of the rock mass. While the number of temperature sensors is very high, only eight gas pressure and eight relative humidity sensors are installed in the SHT block. The relative humidity sensor indirectly measures the moisture content in the rock pores. In addition to passive monitoring by relative humidity sensors, the moisture content is also measured through active testing by neutron logging, electrical resistivity tomography, cross-hole ground-penetrating radar tomography, and cross-hole air injection tests. These active tests have been carried out at appropriate intervals in selected boreholes throughout the SHT. The passive monitoring data of pressure and relative humidity, as well as active test data of air injection tests in Boreholes 16 and 18, have been discussed in other project deliverables (Freifeld and Tsang, 1997a; 1997b; 1997c). Similarly, active testing by ground penetrating radar tomography and infrared imaging also have been discussed in other project deliverables (Peterson and Williams, 1997; Cook and Wang, 1997a; 1997b; 1997c)., We shall, therefore, focus here on the complete temperature data set for the interpretation of thermal-hydrological conditions of the SHT.

Many boreholes in the SHT are instrumented with multiple temperature sensors along their lengths, recording hourly temperature. These boreholes are Boreholes 2, 3, 4, 8, 9, 10, 11, 12, which are parallel to Heater Hole 1, collared on the Thermo-mechanical Alcove wall; Boreholes 5, 13, 15, 16, 17, 18, which are orthogonal to Heater Hole 1, collared on the Thermo-mechanical alcove extension wall; and Boreholes 22, 23, 14 which are orthogonal to the Heater Hole 1, collared on the Access/Observation Drift wall. Refer to Figure 2.1 for the layout and borehole arrangement in the SHT. The coordinate system of the boreholes is defined with reference to the collar of Heater Hole 1 at (0, 0, 0). The X axis extends approximately north-south, with the positive X axis pointing south toward the Thermal-mechanical Alcove Extension. The positive Y axis is approximately east. The heater extends from Y = 2 m to Y = 7 m. The temperature data which are available from multiple locations in the above boreholes will allow display of temperature profiles varying with radial distance from the heater at different phases of heating. That the temperature is being continuously monitored during testing will allow the data to be displayed as temperature history for individual sensors. Examination of the temperature data alone can reveal the nature of the heat-transfer processes taking place. For example, if the heat transfer is not purely conductive, but occurs by means of liquid and vapor counter flow (that is, featuring a heat pipe), then the telling signatures in the temperature data will be a small temperature gradient in the heat-pipe region, and that with time the temperature value remains at the nominal boiling point of water.

Figure 2.2 shows a compilation of temperature data from all the boreholes with temperature sensors. The temperature at test times of 1/2 month, 1 month, 2 months, 3 months, 4 months, 5 months, 6 months, 7 months, 8 months, and 9 months of heating is shown as a function of radial distance from the heater. For those boreholes orthogonal to the heater hole, sensors are located at different radial distances from the heater hole. For those boreholes parallel to Heater Hole 1, multiple sensors have different Y coordinates, even though their radial distance from the heater is almost identical. Since the heater extends from Y = 2 to 7 m, those sensors with Y coordinates close to the two ends of the heater will register lower temperatures. Those boreholes with multiple sensors and different Y coordinates, but with the same radial distance from the heater, are labeled in the first graph at t = 1/2 month of heating in Figure 2.2.

3. Interpretation of Measured Temperature Data by Numerical Thermal-Hydrological Simulations

In this section, temperature data to be compared with simulation results will be displayed in two ways. The first display includes the temperature readings from different boreholes as a function of radial distance from the heater, at 9 months of heating. This display is similar to Figure 2.2, but contains only a subset of the data shown in Figure 2.2. For those boreholes that are parallel to the

heater with multiple sensors, each with different Y coordinates, only the temperature with Y coordinate closest to the center of the heater, i.e. Y = 4.5 m, will be included. Similarly, for those boreholes orthogonal to the heater hole, only temperature in Boreholes 15, 16, 17, 18 which lie in the plane with Y coordinate closest to Y = 4.5 m are included. The second kind of display is the time history of temperature data from two boreholes parallel to Borehole 1 (heater): Boreholes 2 and 3, again only for the sensor with Y coordinate closest to the center of the heater. Borehole 2, the closest to the heater, is to the south of the heater at a radial distance of 0.34 m. Borehole 3 is at a radial distance of 0.68 m to the north of the heater. Temperature data for all sensors in individual boreholes, at different phases of heating, will be compared to simulations in Section 4, below.

Case 1 Simulated Results (Baseline Model)

Pretest predictions of the SHT were reported in Birkholzer and Tsang (1996). The readers are referred to that report for details regarding conceptual model, problem definition, and simulation methodology. As a first step in the interpretation of the measured data, we compare the data to the predictions in the pretest analysis. The pretest analysis is repeated here with a few modifications, as follows: First, the discretization grid is refined from that used in the pretest analysis, particularly near the heat source: it has radial increments starting as small as 0.02 m at the Heater Borehole 1, increasing to 0.05 m at the radial distance of 1 m from the heater, to 0.2 m at the radial distance of 2 m from heater borehole 1, and to about 0.5 m at 5 m distance from the heater. The number of grid blocks used in the simulations presented here is 14,796 as compared to 9,016 in Birkholzer and Tsang (1996). Second, vapor pressure lowering effects due to capillary and phase adsorption effects are included in the present simulations. Although vapor pressure lowering only very slightly affects the average temperature values, it plays an important role in smoothing artificial oscillation of pressure and temperature values arising from numerical effects due to discretization. Since the diagnostic signatures for different heat transfer mechanisms are often subtle variations of slope in the temperature curves, it is important to have smooth simulated results. Both the grid refinement and inclusion of vapor pressure lowering effect are intended to minimize unwanted gridding effects in the simulated results, in order to avoid erroneous conclusions in interpreting test results. The other two simulation modifications reported here are in the incorporation of more current data not available to us at the time of pretest analysis. One is in the adjustment of the rock mass heat capacity from 928.0 J/(Kg °K) to 953.0 J/(Kg °K) (Brodsky et al., 1997). The other is the use of the 9-month average of the heater power (3758 W) instead of the 1-month average value of 3861 W from the pretest analysis.

In Figures 3.1 and Figure 3.2, we compare measured temperature data to the simulated results at the end of the 9-months heating phase of the SHT. The simulated results are based on the predictions in Birkholzer and Tsang (1996) with the above mentioned modifications. Figure 3.1 shows the temperature as a function of radial distance from the heater hole, at approximately the

midpoint of the heater, y = 4.25 m, and Figure 3.2 shows the time evolution of temperature in Boreholes 2 and 3, parallel to Heater Borehole 1, also at y = 4.25 m. Note that in Figure 3.1, the greatest discrepancy between the predictions and the measurements is at radial distances between 1.25 m and 3 m. This is not surprising, since for this case, a uniform thermal conductivity of 1.67 W/(m °K), independent of liquid saturation and temperature, was employed. The value 1.67 was that of air-dried core samples from the SHT boreholes, which were the only laboratory measurements of site specific samples available at the time of pretest analysis. While the thermal conductivity of 1.67 W/(m °K) may adequately represent the actual thermal conductivity of the dry-out zone (~ 1 meter around the heater), it greatly underestimates the thermal conductivity elsewhere, since it is known that the thermal conductivity of welded tuff increases with liquid saturation, and since the ambient liquid saturation of the SHT is expected to be on the order of 0.92, and even higher in the condensation zone (between about 1 to 3 meters from the heater). The underestimation of the thermal conductivity gives rise to the overprediction of temperature by simulations as shown in Figure 3.1. The temperature overprediction by the parameters used in the baseline model was anticipated (Birkholzer and Tsang 1996).

Figure 3.2 displays the time history of temperature in Boreholes 2 and 3, both parallel to Heater Hole 1, at radial distances of 0.34 m and 0.68 m respectively. The figure shows that even in the dry-out zone, the temperature is still overestimated by the simulation. The measured data in both Borehole 2 and 3 indicate a brief pause at the nominal boiling point – at around 15 days after heating in Borehole 2 and at around 50 days after heating in Borehole 3. The plateau of temperature at the nominal boiling point signifies the presence of liquid and vapor counterflow. The effect is more distinct for Borehole 2 and much more subtle for Borehole 3. It is clear from Figure 3.2 that the simulations predict a more prominent heat pipe of longer time duration than the more subtle effect shown in the data.

Simulations with different input parameters will be performed to calibrate the numerical model with the measured data. Table 3.1 lists the input parameters of the different sets of simulations.

Table 3.1 Input Parameters for Different sets of Simulations

Simulation Case	Description of input parameters
Case 1 (Baseline)	Material properties as those in Birkholzer and Tsang (1996) Uniform thermal conductivity K = 1.67 W/(m °K)
Case 2	Same material properties as Case 1, except K varies as square root of liquid saturation, C_{dry} =1.67 W/(m °K), and C_{wet} = 2.0 W/(m °K)
Case 3	Same material properties and thermal conductivity as Case 2 Background fracture continuum permeability is one order of

Simulation Case	Description of input parameters
	magnitude smaller than in Cases 1 and 2, namely 5.85 x 10^{-15} m^2
Case 4	Same material properties as Case 1 except K varies as square root of liquid saturation, C_{dry}=1.35 W/(m °K), and C_{wet} = 2.1 W/(m °K) Same low background fracture continuum permeability of 5.85 x 10^{-15} m^2 as in Case 3
Case 5	Same material properties as Case 1 Heat conduction only, no thermal-hydrological coupling Uniform thermal conductivity K = 1.67 W/(m °K)
Case 6	Same material properties as Case 1 Heat conduction only, no thermal-hydrological coupling Uniform thermal conductivity K = 2.0 W/(m °K)
Case 7	Material properties are not that of Case 1, but are calibrated to liquid saturation and moisture tension for Borehole SD-9 with a percolation flux of 3.6 mm/yr, These are the parameters used for pretest simulations for the Drift Scale Test (Birkholzer and Tsang, 1997). Fracture Permeability is the same as Case 1, from characterization data of SHT K varies as square root of liquid saturation, C_{dry}=1.67 W/(m °K), and C_{wet} = 2.0 W/(m °K)

Case 2 Simulated Results - More Realistic Liquid-Saturation-Dependent Thermal Conductivity

The first step in the calibration effort is to use a more realistic set of thermal conductivity values to simulate the SHT. Therefore, for Case 2 here, the original value of K = 1.67 W/(m °K) is retained to represent the thermal conductivity for a dry rock mass, C_{dry}, but a higher value of C_{wet} = 2.0 W/(m °K) is assumed for that of a saturated rock mass (N. Brodsky, personal communication, while laboratory measurements of SHT core samples were still in progress, non-Q). A square root dependence of the thermal conductivity with liquid saturation is assumed:

$$K = C_{dry} + \sqrt{S_\ell}(C_{wet} - C_{dry}) \qquad (1)$$

Except for this modification, all other input parameters were identical to those of Case 1. Figures 3.3 and 3.4 show the comparison of measured data with the simulations. It is apparent that the temperature match between simulations and measurements is much improved over that of Case 1 (cf. Figures 3.1 and 3.2). However, the transient heat-pipe effect at early times, before heat

conduction takes over, remains more prominent in the simulations than in the measured data. Since the heat-pipe phenomenon depends on both the flow of vapor (mostly in the fractures) away from the heated region, and the return flow of liquid water (in both the matrix and fractures), the key parameters controlling the heat-pipe effect will be the matrix and fracture permeability. To illustrate this dependence, the SHT may be simulated with a different fracture permeability, as discussed in the next case.

Case 3 Simulated Results - Effect of Fracture Permeability

Air permeability characterization of the SHT block prior to heating shows that the permeability to air for different boreholes ranges from 5.0×10^{-15} m^2 to 5.2×10^{-12} m^2. The combined data of fracture mapping in the SHT block, borehole video logs, and air injection interference tests indicate the presence of a high permeability fracture zone intersected by the boreholes that give the highest permeability values in the 10^{-12} m^2 range. The baseline model in Birkholzer and Tsang (1996) therefore includes a vertical high permeability fracture zone, 4 m in extent to the south of the heater hole, making an angle of 22° with the X axis and centered about Y = 5.5 m. This fracture zone is given the higher fracture permeability of 5.2×10^{-12} m^2. Since air permeability estimation for many boreholes give much lower values, and since their interference pressure response indicates the fractures are well connected, the baseline model of Birkholzer and Tsang (1996) treats the fractures as a continuum and assigns a lower background permeability of 5.8×10^{-14} m^2 (the median of all the measured air permeability values for individual boreholes) for most of the SHT block.

Based on the range of measured permeability values obtained from the air permeability tests in different boreholes, and based on the observation that when the borehole is isolated into shorter zones, the pressure response to air injection test in some zones exhibits almost impermeable behavior, it is plausible that the background fracture continuum permeability may be lower than the value assumed for the earlier simulations. For this case, then, the low background fracture permeability is given a value of an order of magnitude lower, namely 5.8×10^{-15} m^2. The adjustment of fracture permeability is expected to affect the liquid and vapor counterflow behavior.

The results are shown in Figures 3.5 and 3.6. As anticipated, the biggest difference of the simulated results from previous cases is in the reduction of heat-pipe behavior, seen in Figure 3.6. Now the match to the data in Borehole 3 is much improved. On the other hand, the match of the simulations to the data in Borehole 2 is worse than in the previous cases because of the more distinct heat-pipe signature in the data. It should be pointed out that Borehole 3 is to the north of the Heater Hole 1, and air injection tests in Boreholes 22 and 23 to the north of the heater block give the lowest air permeability values of 10^{-15} m^2. This may account for the very weak heat-pipe effect in the Borehole 3 data reproduced by the Case 3 simulations, while a more prominent heat-

pipe effect in Borehole 2 data is better represented by the Case 2 simulations, which employs a higher fracture permeability. These results show that the presence and absence of heat-pipe effects in the measured data may be sensitively affected by the local heterogeneity of the fracture permeability. They suggest that a more refined heterogeneous structure of the fracture permeability than the present conceptual model contains may be required to reproduce the subtle spatial variability of the thermal-hydrological response in different boreholes. Inverse modeling of all pretest air injection test interference data can provide a more refined heterogeneous fracture model.

Case 4 Simulated Results - Effect of Further Refinement on Thermal Conductivity Values

It is clear from the discussion so far that the overall temperature values are controlled by the thermal conductivity parameter, but to resolve the different heat-transfer mechanisms requires close examination of subtle variations and inflections in the slope of temperature data. This also underlines the importance of grid design and grid refinement so that the geometry of grids would be compatible with the expected parameter contours, and that no numerical artifacts are present to obscure the real physical effects. To demonstrate the effect of thermal conductivity values on the fit of simulations to data, a further refinement of the thermal conductivity parameters will be carried out. The parameters chosen are C_{dry} = 1.35 W/(m °K) for totally dry rock mass and C_{wet} = 2.1W/(m °K) for fully saturated welded tuff. The rationale is as follows. The higher value of C_{wet} = 2.1W/(m °K) was chosen for two reasons. First, the new value is based on more recent laboratory measuremnts of SHT core samples (personal communication, Nancy Brodsky, non-Q); the second reason is that the comparison of the data with predictions from Cases 2 and 3 parameters seem to indicate the need for a higher thermal conductivity in regions with high liquid saturation. The lower value of C_{dry} = 1.35 rather than the 1.67 for previous cases is chosen because the laboratory measurement of 1.67 is performed with air-dry and not totally dry samples. With the present choice of C_{wet} and C_{dry}, Equation (1) will give the value K = 1.67 W/(m °K) at the residual liquid saturation of S_l = 18%.

The comparison of measured data and simulations are presented in Figures 3.7 and 3.8. While in Figure 3.7, the match between data and simulations seems to improve over that in Figure 3.5, the fit to the temperature history at late times in Borehole 3 seems to be worse in Figure 3.8 than in Figure 3.6. Not shown here are the match for the complete set of temperature data in all the boreholes instrumented with temperature sensors. An examination of temperature results for all the boreholes indicate that while for some boreholes the match is closer with Case 4 parameters, in other boreholes the match is better with Case 3 parameters. There is not a clear indication that one set of thermal conductivity parameters is preferable to the other. Given the spatial heterogeneity of the properties (such as fracture permeability) in the SHT block which can give rise to spatial dependence of thermal-hydrological response, a further refinement of "wet" and "dry" thermal conductivity values does not seem warranted.

Case 5 and Case 6 Simulated Results - Significance of Thermal-Hydrological Coupling

The dramatic improvement in the fit between simulated results and data from Case 1 to all subsequent Cases (where more realistic liquid saturation dependent thermal conductivity parameters were utilized) clearly demonstrates the importance of the thermal conductivity parameter in controlling the thermal response of the SHT. However, while conduction is no doubt the dominant heat transfer mechanism, and the effect of thermal-hydrology coupling seems minor and subtle, the latter cannot be ignored in the interpretation of data. To illustrate, simulations were run with heat conduction alone, first with the constant thermal conductivity of K =1.67 W/(m °K), the value corresponding to the laboratory measurements of air-dry samples from the SHT. Figures 3.9 and 3.10 show the results. It is clear that though the thermal conductivity values are consistent with those in the dry-out zone, the simulated results grossly overpredict the measured data everywhere. The conduction-only simulations were repeated with the uniform thermal conductivity of K = 2.0 W/(m °K), the value corresponding to the *in situ* REKA probes – Rapid Estimation of K and α estimation – for the rock mass (personal communication, Robin Datta, non-Q). The results are shown in Figures 3.11 and 3.12. The simulated results still overpredict the measured data, demonstrating that thermal hydrological coupling accounts for a notable fraction of heat transfer away from the heated region by convection. Obviously, in the absence of thermal-hydrological coupling, the subtle heat-pipe signature evidenced in the data is missed in these heat-conduction-only simulations of Figures 3.10 and 3.12.

Case 7 Simulated Results - Effect of Percolation Flux

For all the above (Cases 1-6), only the values of thermal conductivity and background fracture continuum permeability have been varied in the interpretation of the SHT temperature data. The matrix and fracture properties are fixed to conform to the baseline model used in the predictive analysis of the SHT (Birkholzer and Tsang, 1996). On the other hand, two different sets of matrix and fracture properties were used in the predictive analysis of the larger Drift Scale Test (Birkholzer and Tsang, 1997). These were based on the calibration studies by inverse modeling from the Unsaturated Zone Site Scale Model (Bodvarsson et al., 1997). Since SD-9 is the well closest to the DST area, properties in the Drift Scale Test analysis correspond specifically to parameters derived from the calibration against the liquid saturation and moisture tension in Borehole SD-9. In that calibration, the matrix and fracture properties correspond to a percolation flux of 3.6 mm/yr. SD-9 is located near the breakout from the ESF Main Drift to the thermal test alcove, which houses both the SHT and the DST. For the Case 7 study here, we employ the matrix and fracture hydrological properties used in the Drift Scale Test analysis. However, the thermal conductivity values were kept identical to those of Case 2, and so is the fracture permeability structure, (that is, a high permeability fracture zone superimposed on a background of low permeability of 5.8×10^{-14} m^2). The simulated results and their comparison to data are shown in Figures 3.13 and 3.14. These should be compared to Figures 3.3 and 3.4 of Case 2. Note the underprediction of temperature in the dry-out region ($r < 1.0$ m) in Figure 3.13, and the

overprediction of the length of heat pipe in Figure 3.14. The difference in the simulated results between Case 2 and Case 7 arises from the different matrix and fracture properties, as shown in Table 2.

Table 2. Hydrological Properties of Matrix and Fracture in the middle non-lithophysal unit of Topopah Spring Welded Tuff

Parameter	Single Heater Test Baseline Model, Cases 1-6	Case 7 - 3.6 mm percolation flux, calibrated for the DST
Matrix Permeability (m^2)	4×10^{-18}	9.14×10^{-18}
Fracture Permeability (m^2)	1×10^{-12} for fracture zone 5.8×10^{-14} background, for Cases 1, 2, 5, 6 5.8×10^{-15} background for Cases 3, 4.	Same as SHT Cases 1, 2, 5, 6 1×10^{-12} for fracture zone 5.8×10^{-14} background
Matrix Van Genuchten Parameter α (Pa^{-1})	6.4×10^{-7}	0.171×10^{-5}
Fracture Van Genuchten Parameter α (Pa^{-1})	$1. \times 10^{-3}$	0.217×10^{-4}
Matrix Van Genuchten Parameter β	1.47	1.47
Fracture Van Genuchten Parameter β	1.47	1.93
Matrix residual saturation	0.18	0.18
Fracture residual saturation	0.01	0.01
Fracture liquid saturation (Pre-Heat) S_{lf}	0.052	0.15
Matrix Liquid Saturation (Pre-Heat) S_{lm}	0.92	0.92

The matrix and fracture properties in the third column are calibrated values appropriate for a percolation flux of 3.6 mm/yr. These give rise to higher matrix liquid permeability as well as higher initial (pre-heat) fracture liquid saturation as compared to those given by the SHT baseline

model in Column 2 of Table 2. The initial (pre-heat) fracture liquid saturation is 5% in the second column, and 15% in the third column. The higher liquid permeability and fracture liquid saturation of Case 7 parameters give rise to more effective convective heat transfer and account for the lower predicted temperature in the dry-out zone shown in Figure 3.13, and the more prominent and longer duration heat-pipe effect shown in Figure 3.14. The lower fracture liquid saturation of 5% in the SHT baseline model is more commensurate with a lower percolation flux. Therefore, the SHT data seem to support a percolation flux smaller than 3.6 mm/yr.

4. Comparison of Temperature Data with Case 4 Simulations at Different Phases of Heating

In Section 3 above, the suite of simulations with different thermal and hydrological parameters was compared to the measured temperature at the end of the 9-month heating phase. Also, the time evolution of temperature was shown for only two boreholes. Both are parallel to the heater and are close enough to lie within the dry-out zone for the majority of the heating phase. In this section, comparison of simulations to a more complete data set will be presented for Case 4. For those boreholes with multiple temperature sensors, results will be shown for the readings on all sensors, at 1 month, 3 months, and 9 months of heating. For those boreholes that are parallel to the heater hole, sensors placed along the borehole have different Y coordinates, therefore the measured and the simulated temperature will be plotted as a function of Y coordinate, where the markers show the actual location of the sensors, and the simulated results are curves with no markers. The boreholes parallel to the heater hole are Boreholes 2, 3, 4, 8, 9, 10 and 11, and the results are shown in Figures 4.1 through 4.7. For those boreholes orthogonal to the Heater Hole 1, the Y coordinates are somewhat constant, and the multiple sensors placed along the hole have different X coordinates, and thus the measured and simulated temperatures are plotted as a function of X coordinate. Again, the markers show the actual location of the temperature sensors, and the simulated results are curves with no markers. The boreholes orthogonal to Heater Hole 1, with Y coordinates close to the mid-point of heater, are boreholes 15, 16, 17, 18. The results are shown in Figures 4.8 through 4.11. Figures 4.1 through 4.11 show that the simulated results, at some sensor locations and at some phases of heating, overpredict the measurement; while at other sensor locations and at some other phases of heating, they underpredict the measurements. Overall, the agreement of simulated results and measurements is fair. One may attribute the discrepancy of prediction and data in part to spatial heterogeneity of the properties in the rock mass.

One puzzling feature is the asymmetry of temperature about the mid-plane orthogonal to the heater axis seen in Figure 4.1. For Borehole 2, it is clear that the temperature toward the back (Y > 4.5 m) of the SHT block is lower than the temperature toward the front (Y < 4.5 m) of the test

block. The drop of temperature data for Y > 6 m is particularly dramatic. Since the baseline conceptual model of the SHT has a high permeability fracture zone between 5 and 7 m, it was thought at first that the high-permeability zone with $k = 5.8 \times 10^{-12}$ m^2 would serve as an effective conduit to channel air away from the heater, and then through the background continuum air permeability vent to the thermal-mechanical alcove extension drift wall, resulting in cooler temperatures for Y > 5 m. However, it is clear from Figure 4.1 that there is little drop in temperature in the simulated results for Borehole 2. Our simulations typically show asymmetry about Y = 4.5 m for gas pressure and liquid saturation, but not for the temperature distribution. To further probe the effect of communication with the Thermal-mechanical Alcove Extension drift wall, the high-permeability zone in the baseline conceptual model was extended all the way to the drift wall, and simulations were carried out for Cases 2 and 3. In addition, the entire back portion of the simulated block for Y > 5 m was given the high fracture continuum permeability of 5.8×10^{-12} m^2 and simulations were repeated for Cases 2 and 3. The assumed higher fracture continuum permeability does not seem to have much impact on the simulated temperature. Therefore, heterogeneity in fracture permeability alone cannot account for the large asymmetry in temperature about Y = 4.5 m observed in the data for Borehole 2. Other than this particular puzzling feature, it seems that the thermal-hydrological response of the SHT is well understood and well represented by the numerical models.

5. Interpretation of Active Testing Data

Since active test results have been reported separately in other Level 4 deliverables – Freifeld and Tsang (1997a, 1997b; 1997c) for air injection tests in Boreholes 16 and 18; Peterson and Williams (1997) for ground penetrating radar tomography using boreholes 15, 17, 22 and 23 – only a brief summary of active testing data interpretation of will be presented here.

Both air injection tests and radar tomography are intended to probe the redistribution of moisture in the rock mass due to heating. In Figures 5.1 and 5.2 based on Case 4 input parameters, the simulated time evolution of the liquid saturation for rock matrix and fractures (at t = 1/2 month, 3 months and 9 months of heating) as a function of distance from the heater along Boreholes 16 and 18 are shown. Note in these figures that there is a build up of liquid saturation in the "condensation zone" extending from the bottom of the borehole at ~ 1.25 and 1.5 m from the heater to about 3 m from the heater. Borehole 16 and 18 both lie just short of the drying zone of about 1 m around the heater as predicted by the simulations (Birkholzer and Tsang, 1996).

Air injection tests in Borehole 16 and 18 were carried out before heating in August 1996, then periodically during heating on November 25, 1996 (Freifeld and Tsang, 1997a), February 4 (Freifeld and Tsang, 1997b) and May 22, 1997, just six days before the termination of heating

(Freifeld and Tsang, 1997c). Permeability values were estimated from the pressure response to constant flow air injection in different zones isolated by high-temperature packers in boreholes 16 and 18. The measurements show that the air permeability values corresponding to the simulated "condensation zone" had a reduction factor of 4 in Borehole 16, and a reduction factor of 2 in Borehole 18, from their pre-heat conditions to November 25, 1996 at 3 months of heating. Permeability values in zones outside of the simulated "condensation zone" show little change from their pre-heat values. Furthermore, measurements carried out in February 1997 and May 1997 indicate that there is little change in the permeability values from November 1996 onwards, whether within or outside of the simulated "condensation zone." These measured results are consistent with the simulated fracture liquid saturation shown in Figures 5.1 and 5.2, where most of the increase in fracture liquid saturation in the "condensation zone" occurs within the first 3 months of heating.

Ground penetrating radar surveys were carried out on August 22, 1996, before heater turn-on in the SHT, and periodically during heating, on January 15, 1997 after 4 1/2 months of heating; March 12, 1997 after 6 1/2 months of heating (Peterson and Williams, 1997). Tomographic inversion of survey data produces velocity fields for each survey. The velocity field changes between surveys, with the greatest changes occurring between the August 1996 pre-heat survey and January 1997 survey. The differences between surveys can be highlighted by inverting the differenced travel times. The travel time for each source-receiver pair from different radar surveys are subtracted, producing three travel time difference data sets: JAN-PRE, MAR-PRE, MAR-JAN, where PRE stands for pre-heat data taken in August 1996. These data sets are then inverted for slowness (inverse of velocity). The JAN-PRE and MAR-PRE tomogram show significant velocity increases and decreases. The increase in velocity occurs around the heater, and the decrease of velocity occurs about 1 m away from the heater toward the alcove walls. The MAR-JAN tomogram shows only velocity increases. Velocity continues to increase near the heater, but velocity in the area 1 meter from the heater does not decrease any further. The differences in the tomograms can be attributed to changes in both temperature and saturation; the quantitative effect of each on the results is presently undetermined. If the temperature dependence of the dielectric constant was ignored, then the difference tomograms would suggest that liquid saturation decreases near the heater and increases about 1 m away, which is consistent with the thermal-hydrological conditions of a drying zone around the heater and condensation zone commencing at about 1 m from the heater, as predicted by simulations. That the January and March surveys have similar velocity decrease indicates that there is little change in the moisture content of the condensation zone after 4 1/2 months of heating, again consistent with the simulated results as shown in Figures 5.1 and 5.2. Another radar survey was performed in May 1997 at 9 months of heating. The velocity tomogram shows very little change from the previous survey taken in March 1997, indicating that the majority of moisture redistribution has occurred in the first few months of heating.

6. Summary

Interpretation of the passive monitoring data and active testing results have been carried out. The thermal-hydrological responses of the SHT in the 9 months of heating seem to be well understood and well represented by the coupled thermal-hydrological numerical models. While heat conduction accounts for most of the temperature rise, effects of thermal-hydrological coupling cannot be ignored in the interpretation of the measured data. Discrepancies between the data and simulations may in part be attributed to spatial heterogeneity and would require further refinement of the numerical model and calibration against detailed site characterization data. The exercise of matching simulated results to measured data in the interpretation process proved to be extremely helpful in constraining the input parameters of the SHT. In particular, the interpretation so far seems to put a constraint on the percolation flux at the SHT. Provided that the other parameters such as thermal conductivity and fracture permeability are reliable, then the SHT data seem to indicate that the percolation flux at the SHT may be less than 3.6 mm/yr.

7. QA Status of Work

The work performed in this study is documented in Yucca Mountain Project Scientific Notebook YMP-LBNL-YT-JB-H-1A. For input to this study, LBNL has used data collected under an approved YMP QMP. The software packages used in this study include standard spreadsheets and visualization and plotting programs. Such programs are not subject to QA requirements under QARD Rev. 7. The software used to simulate thermal-hydrological conditions in the Single Heater Test is the TOUGH2 code (Pruess, 1987, 1991). This program has been qualified under an approved YMP QAP (Pruess et al., 1996; Wu et al., 1996).

The conclusions of this report are mainly based on qualified data and qualified software. The data used for the 1-D SD-9 calibration are Q, as are most of the additional hydrological and thermal data. Site-specific data of the thermal testing area are incorporated whenever possible, and are Q unless designated otherwise.

No data is produced from this work.

Acknowledgment

We thank Stefan Finsterle and Christine Doughty for their review of the manuscript and comments for improvement. Assistance from Melani Menendez-Barreto in graphics is gratefully

acknowledged. This work was supported by the Director, Office of Civilian Radioactive Waste Management, U.S. Department of Energy, through Memorandum Purchase Order EA9013MC5X between TRW Environmental Safety Systems, Inc. and the Ernest Orlando Lawrence Berkeley National Laboratory, under Contract No. DE-AC03-76SF00098.

References

Birkholzer, J.H. and Y.W. Tsang, 1996. Forecast of thermal-hydrological conditions and air injection test results of the Single Heater Test. Yucca Mountain Site Characterization Project Milestone SP918M4 for WBS 1.2.3.14.2, ACCN: MOY-970521-04, Lawrence Berkeley National Laboratory, Berkeley, CA.

Birkholzer, J.H. and Y.W. Tsang, 1997. Pretest analysis of the thermal-hydrological conditions of the ESF Drift Scale Test. Yucca Mountain Site Characterization Project Milestone SP9322M4 for WBS 1.2.3.14.2, ACCN: MOY-970627-12, Lawrence Berkeley National Laboratory, Berkeley, CA.

Brodsky, N.S., M. Riggins, J. Connolly and P. Ricci, 1997. Thermal conductivity and heat capacity measurements for boreholes UE25 NRG-4, UE25 NRG-5, USW NRG-6, and USW NRG-7/7a, SAND 95-1955, DTN:SNL01A05059301.005/NA, Sandia National Laboratories, Albuquerque, NM.

G.S. Bodvarsson, T.M. Bandurraga, and Y.-S. Wu, eds., 1997. The site-scale unsaturated zone model of Yucca Mountain, Nevada, for the Viability Assessment Yucca Mountain Project Milestone Report SP24UFM4, DTN: LB9706001233129.001, LBNL, Berkeley, CA.

Cook, P. and J. Wang, 1997a. Infrared Imaging in the Single Heater Test Area, 1996. Yucca Mountain Site Characterization Project Milestone SP9230M4 for WBS 1.2.3.14.2, ACCN: MOY-970521-01, DTN:LB970100123142.002, Lawrence Berkeley National Laboratory, Berkeley, CA.

Cook, P. and J. Wang, 1997b. Second Quarter Infrared Imaging in the Single Heater Test Area, 1996. Yucca Mountain Site Characterization Project Milestone SP9237M4 for WBS 1.2.3.14.2, ACCN: MOY-970625-04, Lawrence Berkeley National Laboratory, Berkeley, CA.

Cook, P. and J. Wang, 1997c. Third Quarter Infrared Imaging in the Single Heater Test Area, 1996. Yucca Mountain Site Characterization Project Milestone SP9291M4 for WBS 1.2.3.14.2, DTN:LB970700123142.002, LBNL, Berkeley, CA.

Freifeld, B., and Y. Tsang, 1997a. Letter report on first quarter results of measurements in hydrology holes in single heater test area in the ESF. Yucca Mountain Site Characterization

Project Milestone SP9263M4 for WBS 1.2.3.14.2, ACCN: MOY-970513-01, DTN:LB970100123142.001, Lawrence Berkeley National Laboratory, Berkeley, CA..

Freifeld, B., and Y. Tsang, 1997b. Letter report on second quarter results of measurements in hydrology holes in the single heater test area in the ESF. Yucca Mountain Site Characterization Project Milestone SP9216M4 for WBS 1.2.3.14.2, DTN: LB970500123142.001, Lawrence Berkeley National Laboratory, Berkeley, CA.

Freifeld, B., and Y. Tsang, 1997c. Letter report on third quarter results of measurements in hydrology holes in the single heater test area in the ESF. Yucca Mountain Site Characterization Project Milestone for WBS 1.2.3.14.2, DTN: LB970700123142.001, Lawrence Berkeley National Laboratory, Berkeley, CA.

Homuth, F. 1996-1997. Monthly memos to Single Heater Principal Investigators regarding transfer of data from ESF Data Collection Systems, Memorandum LA-EES-13-LV-11-96-041, LA-EES-13-LV-12-96-008, LA-EES-13-LV-01-97-019, LA-EES-13-LV-02-97-019, LA-EES-13-LV-03-97-004, LA-EES-13-LV-04-97-002, LA-EES-13-LV-05-97-017, LA-EES-13-LV-06-97-001, LA-EES-13-LV-07-97-004.

Peterson, J. E., and K.H. Williams, 1997. To assess the effectiveness of the ground penetrating radar method in measuring moisture content in the Single Heater Test. Yucca Mountain Site Characterization Project Milestone SP9241M4 for WBS 1.2.3.14.2, ACCN: MOY-970512-07-A, Lawrence Berkeley National Laboratory, Berkeley, CA.

Preuss, K., 1987. TOUGH user's guide, Nuclear Regulatory Commision Report, NUREG/CR-4645, Lawrence Berkeley Laboratory Report LBL-20700, ACCN:NNA.19890315.0010, Lawrence Berkeley National Laboratory, CA.

Pruess, K., May 1991. TOUGH2 - A general purpose numerical simulator for multiphase fluid and heat flow, Lawrence Berkeley National Laboratory Report LBL-29400, UC-251, ACCN: NNA.1940202.0088, Lawrence Berkeley National Laboratory, Berkeley, CA.

Pruess, K., A. Simmons, Y.S. Wu, and G. J. Moridis, 1996. TOUGH2 software qualification, Lawrence Berkeley National Laboratory Report LBL-38383, UC-814, ACCN: MOL19960610.0010-0020, Lawrence Berkeley National Laboratory, Berkeley, CA.

Tsang, Y.W., J. Wang, B. Freifeld, P. Cook, R. Suárez-Rivera, T. Tokunaga, 1996. Letter report on hydrological characterization of the Single Heater Test area in the ESF. Yucca Mountain Site Characterization Project Milestone OS327322D1, CA. ACCN: MOY-970512-07-B. DTN:LB960500834244.001, Lawrence Berkeley National Laboraotry, Berkeley, CA. Berkeley,

Wu, Y.-S., C.F. Ahlers, P. Fraser, A. Simmons, and K. Pruess, October 1996. Software qualification of selected TOUGH2 modules, Lawrence Berkeley Laboratory Report LBL-39490, UC-800, ACCN:MOL.19970219.0100-0105, Lawrence Berkeley National Laboratory, Berkeley, CA

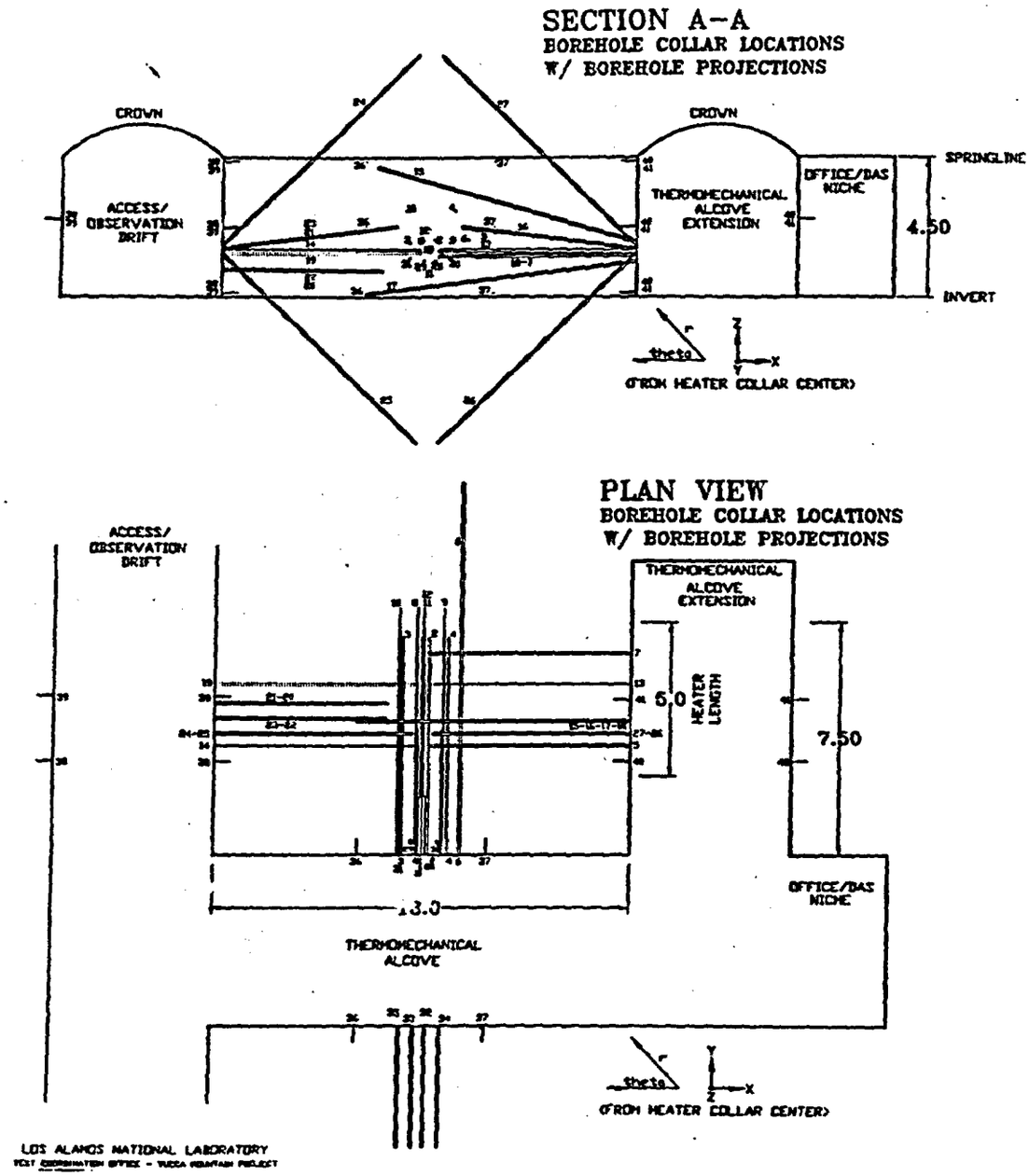

Figure 2.1 Layout and borehole arrangement in the Single Heater Test.

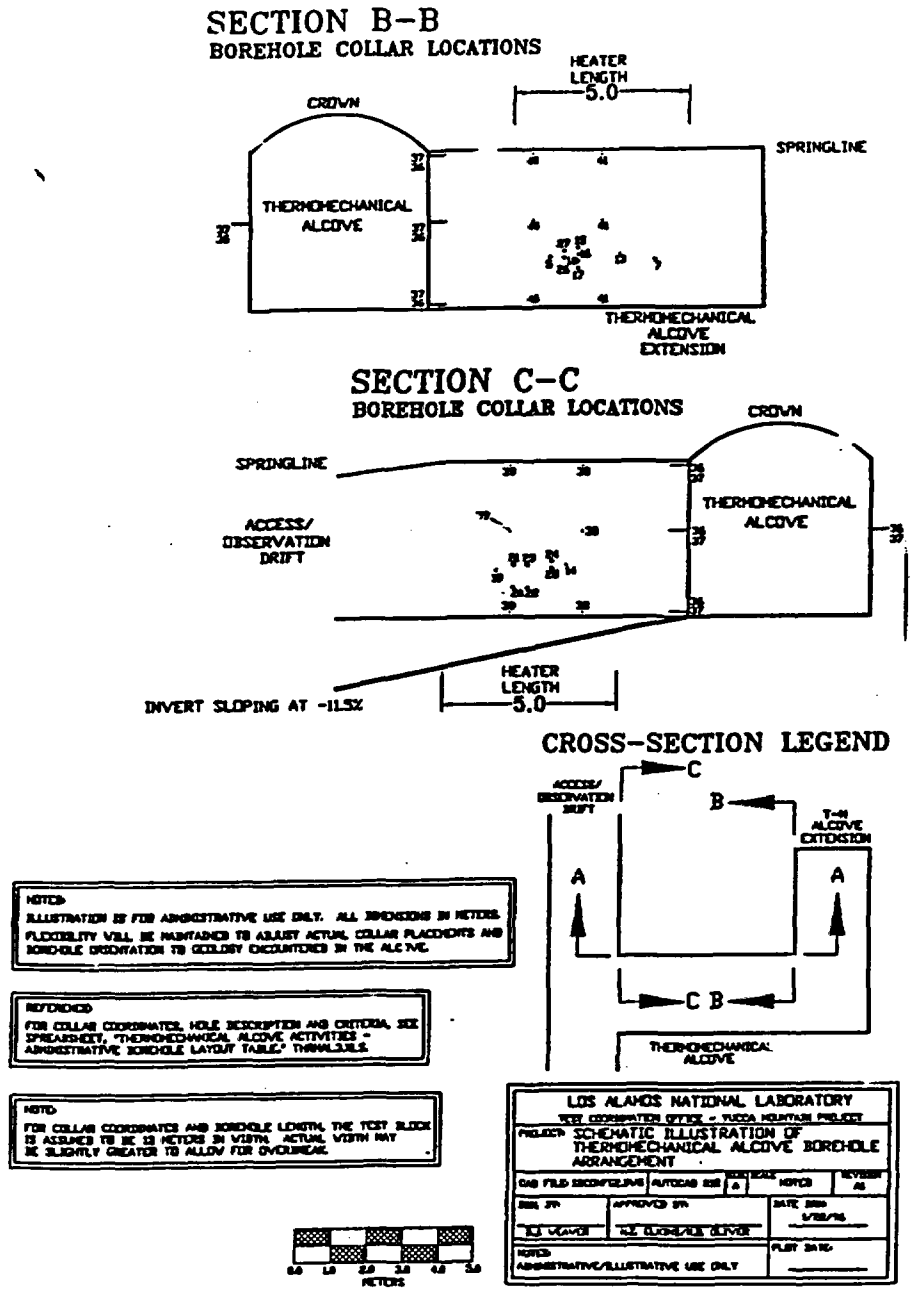

Figure 2.1 (cont.) *Layout and borehole arrangement in the Single Heater Test.*

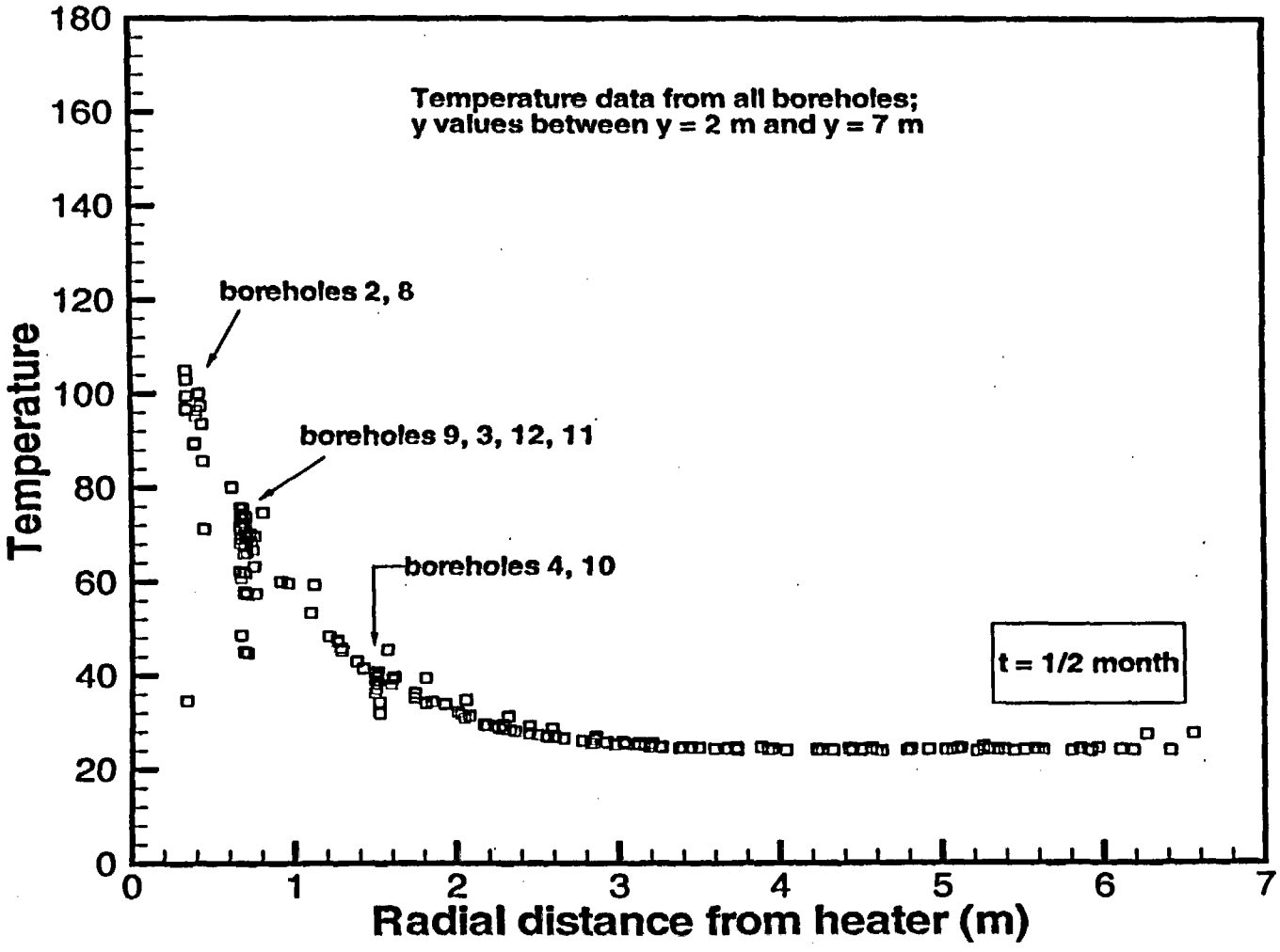

Figure 2.2 Temperature data from boreholes 2, 3, 4, 5, 8, 9, 10, 11, 12, 13, 14, 15, 16, 17, 18, 22, 23

THIS PAGE INTENTIONALLY LEFT BLANK

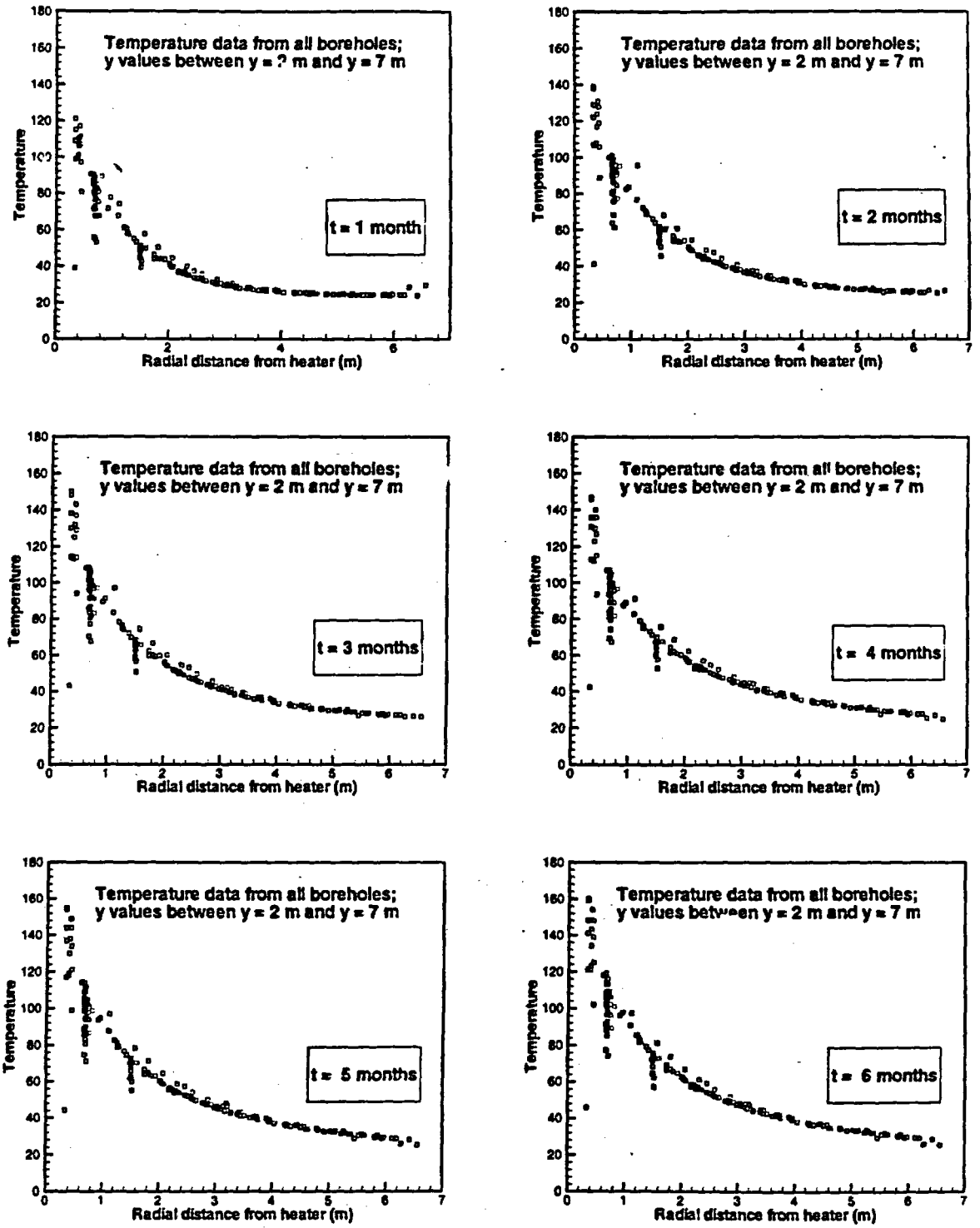

Figure 2.2 (cont.) Temperature data from boreholes 2, 3, 4, 5, 8, 9, 10, 11, 12, 13, 14, 15, 16, 17, 18, 22, 23

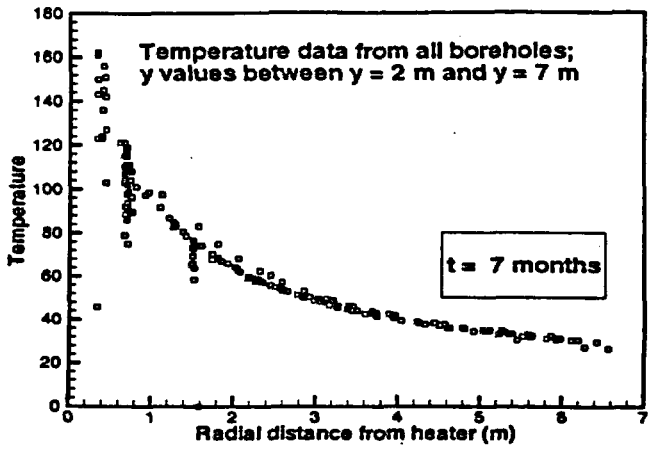

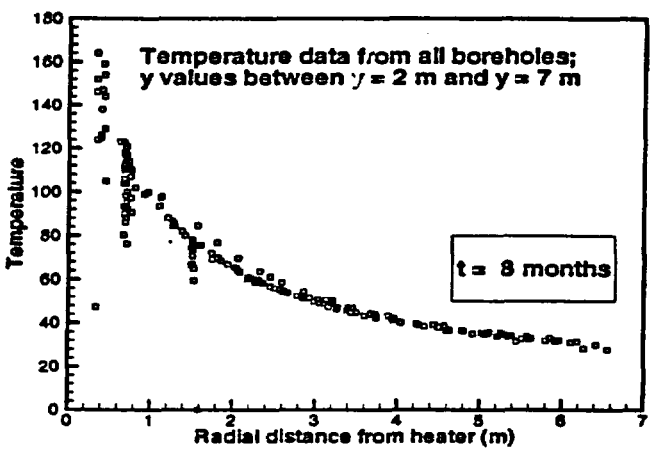

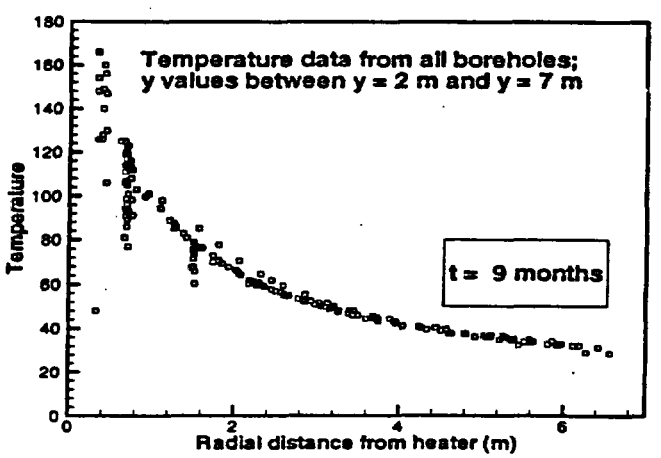

Figure 2.2 (cont.) Temperature data from boreholes 2, 3, 4, 5, 8, 9, 10, 11, 12, 13, 14, 15, 16, 17, 18, 22, 23

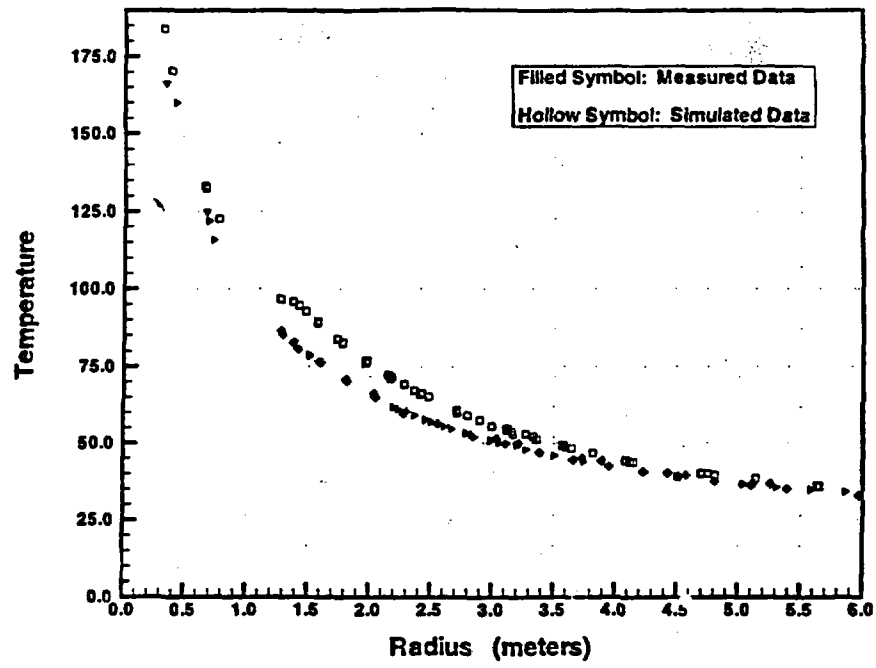

Figure 3.1 *Temperature versus radius for measured and simulated data at t = 9 months, for Case 1, at y = 4.25 m for Boreholes 2, 3, 4, 8, 9, 10, 11, 15, 16, 17, 18*

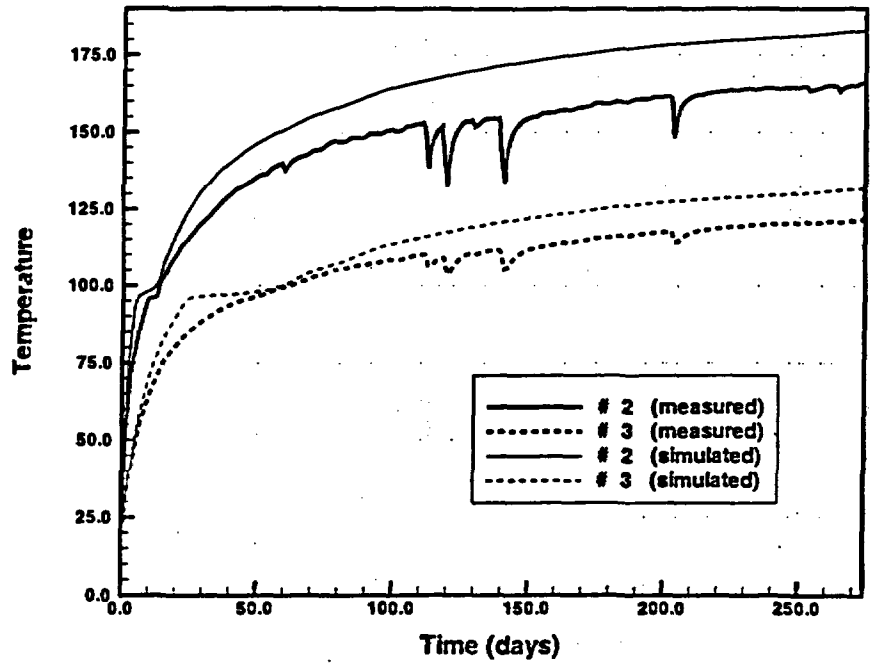

Figure 3.2 *Measured and simulated temperature evolution for Case 1, Boreholes # 2 and # 3 at y = 4.25 m*

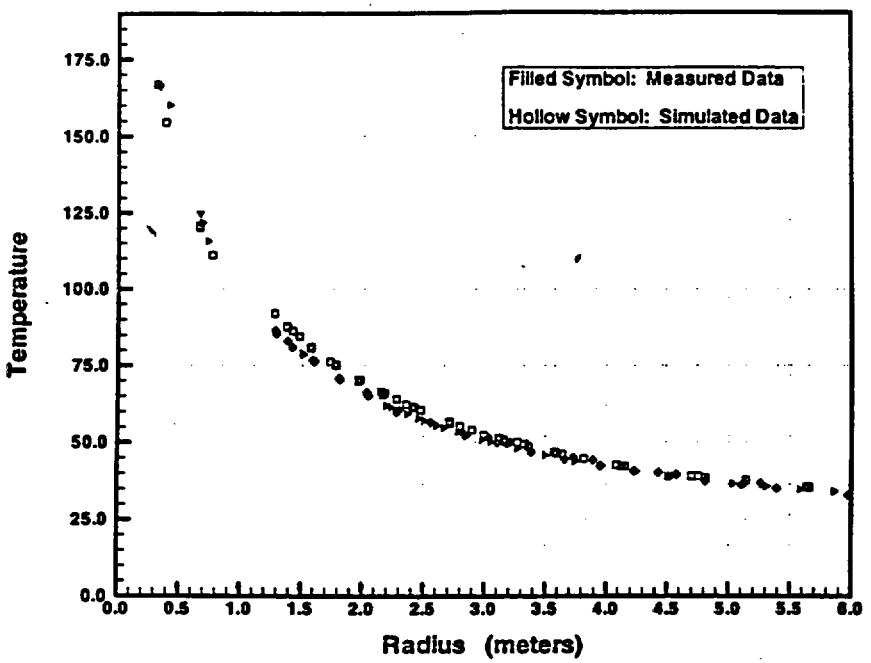

Figure 3.3 *Temperature versus radius for measured and simulated data at t = 9 months, for Case 2, at y = 4.25 m for Boreholes 2, 3, 4, 8, 9, 10, 11, 15, 16, 17,18*

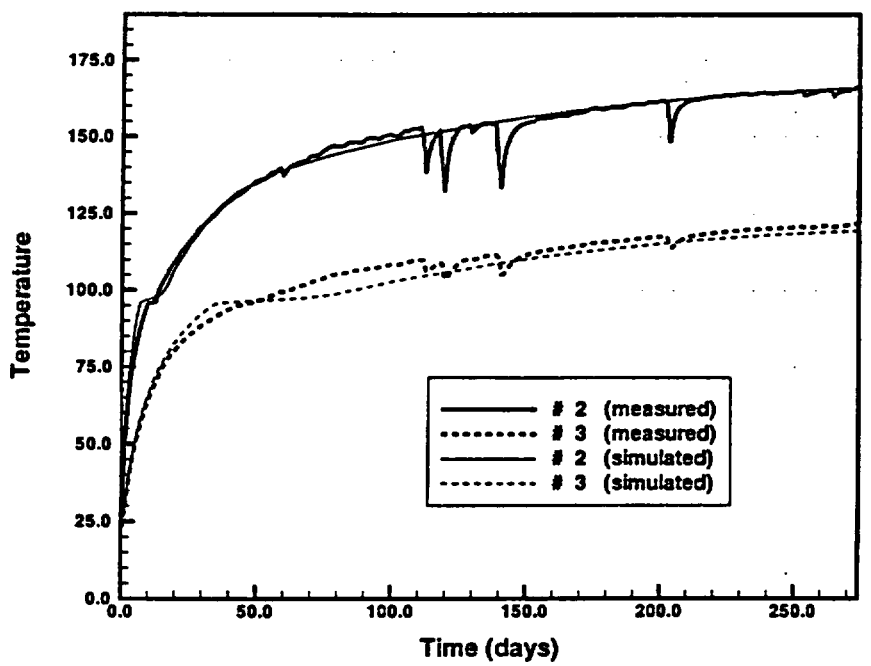

Figure 3.4 *Measured and simulated temperature evolution for Case 2, Boreholes # 2 and # 3 at y = 4.25 m*

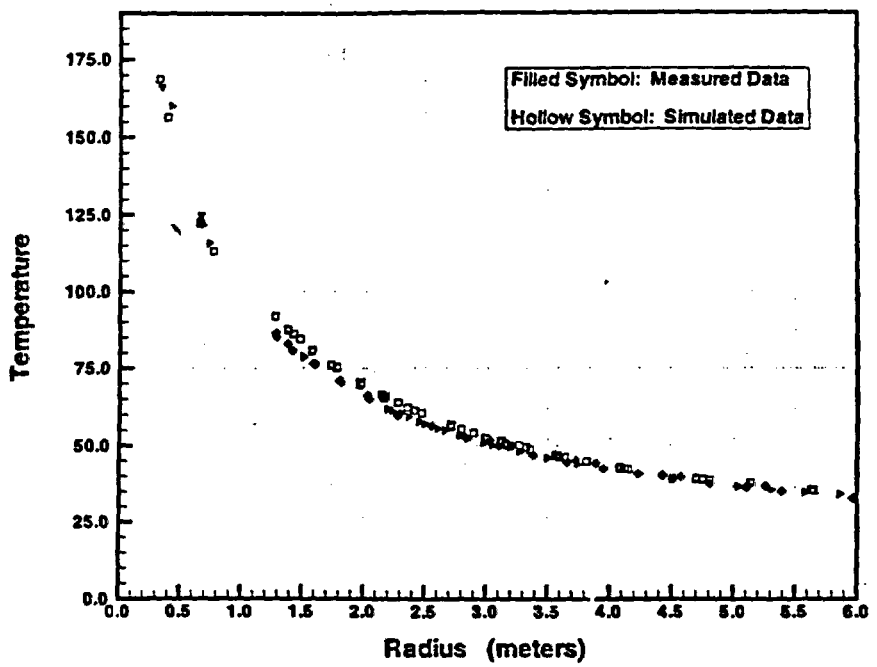

Figure 3.5 *Temperature versus radius for measured and simulated data at t = 9 months, for Case 3, at y = 4.25 m for Boreholes 2, 3, 4, 8, 9, 10, 11, 15, 16, 17,18*

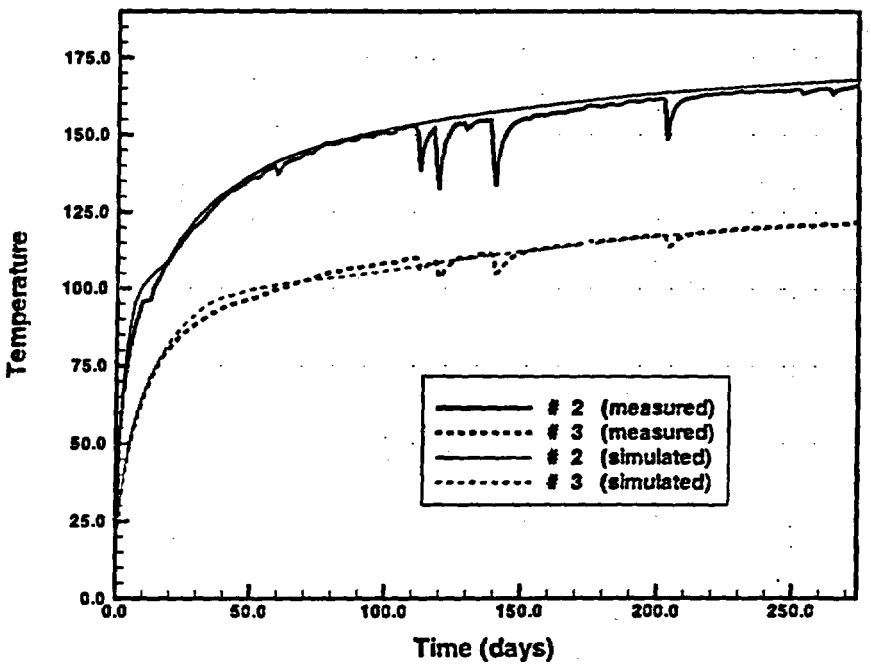

Figure 3.6 *Measured and simulated temperature evolution for Case3, Boreholes # 2 and # 3 at y = 4.25 m*

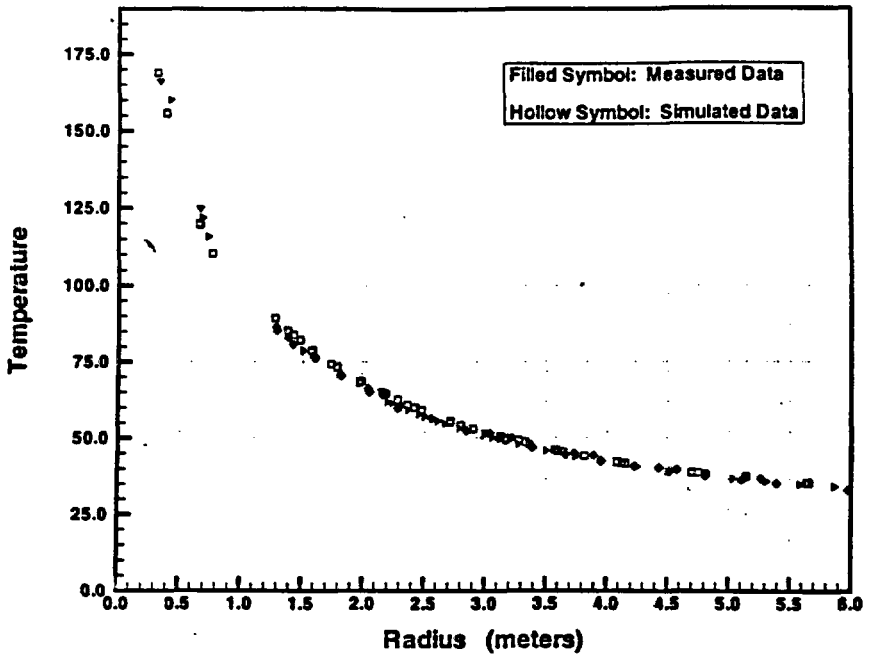

Figure 3.7 *Temperature versus radius for measured and simulated data at t = 9 months, for Case 4, at y = 4.25 m for Boreholes 2, 3, 4, 8, 9, 10, 11, 15, 16, 17,18*

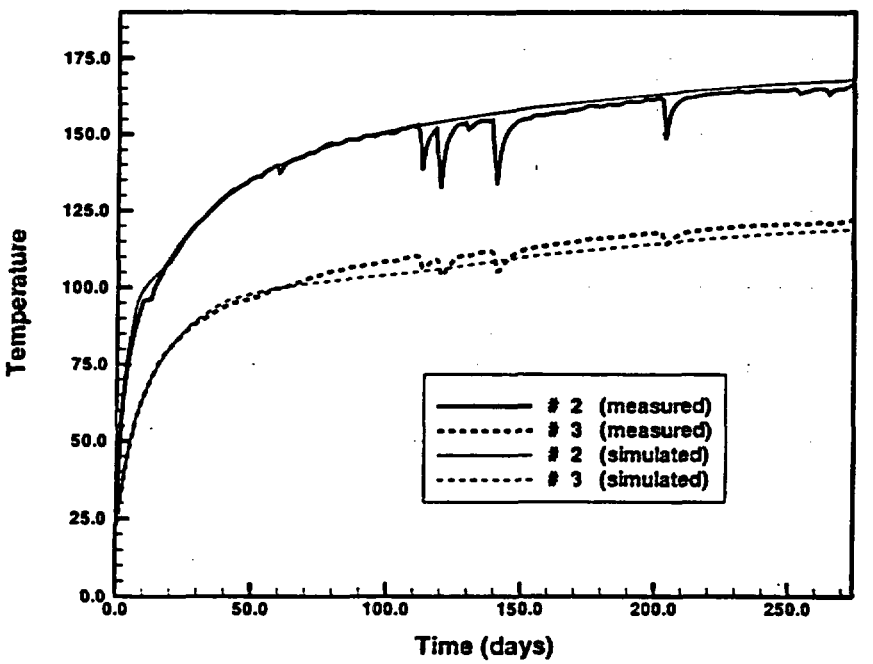

Figure 3.8 *Measured and simulated temperature evolution for Case 4, Boreholes # 2 and # 3 at y = 4.25 m*

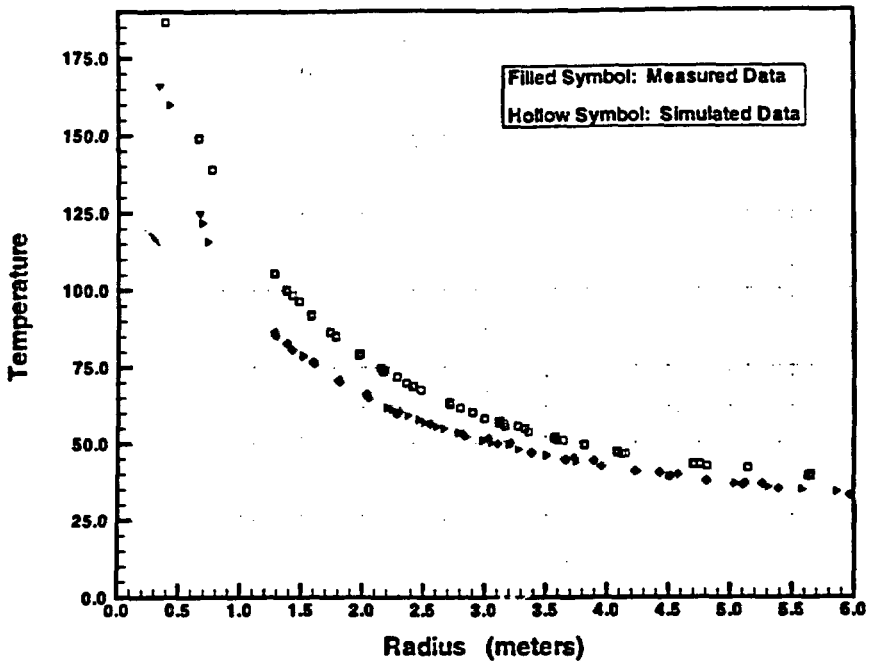

Figure 3.9 *Temperature versus radius for measured and simulated data at t = 9 months, for Case 5, at y = 4.25 m for Boreholes 2, 3, 4, 8, 9, 10, 11, 15, 16, 17,18*

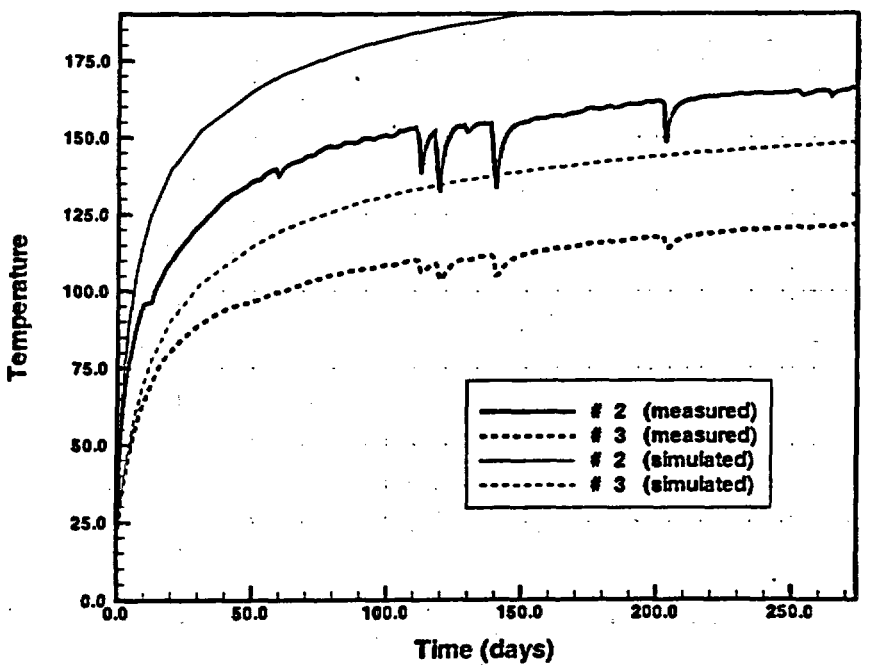

Figure 3.10 *Measured and simulated temperature evolution for Case 5, Boreholes # 2 and # 3 at y = 4.25 m*

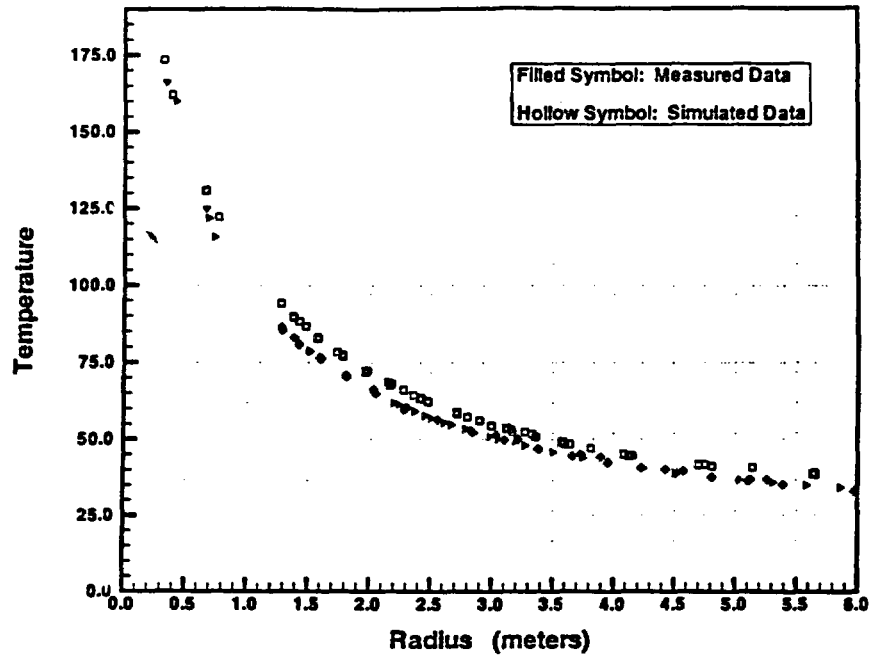

Figure 3.11 *Temperature versus radius for measured and simulated data at t = 9 months, for Case 6, at y = 4.25 m for Boreholes 2, 3, 4, 8, 9, 10, 11, 15, 16, 17,18*

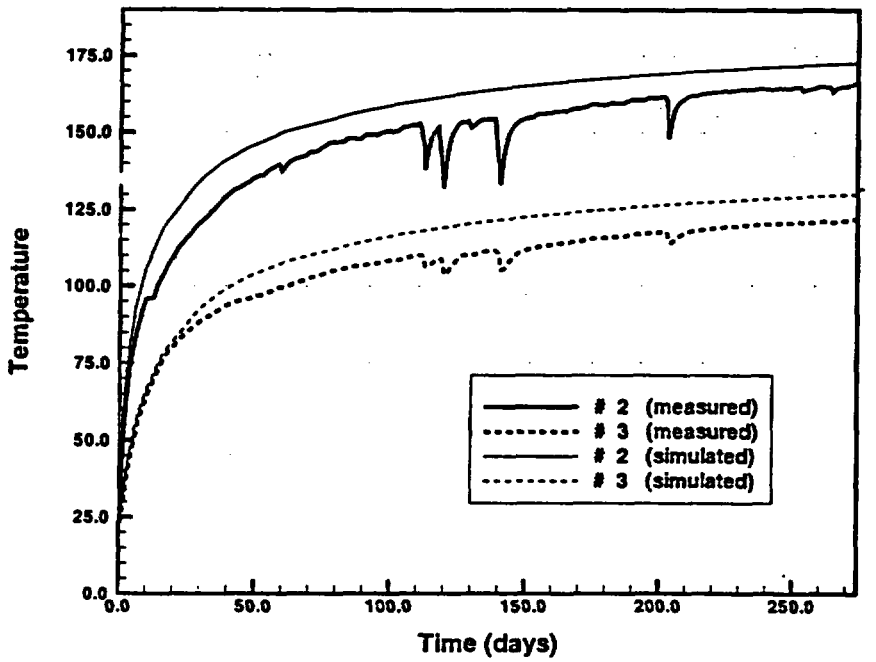

Figure 3.12 *Measured and simulated temperature evolution for Case 6, Boreholes # 2 and # 3 at y = 4.25 m*

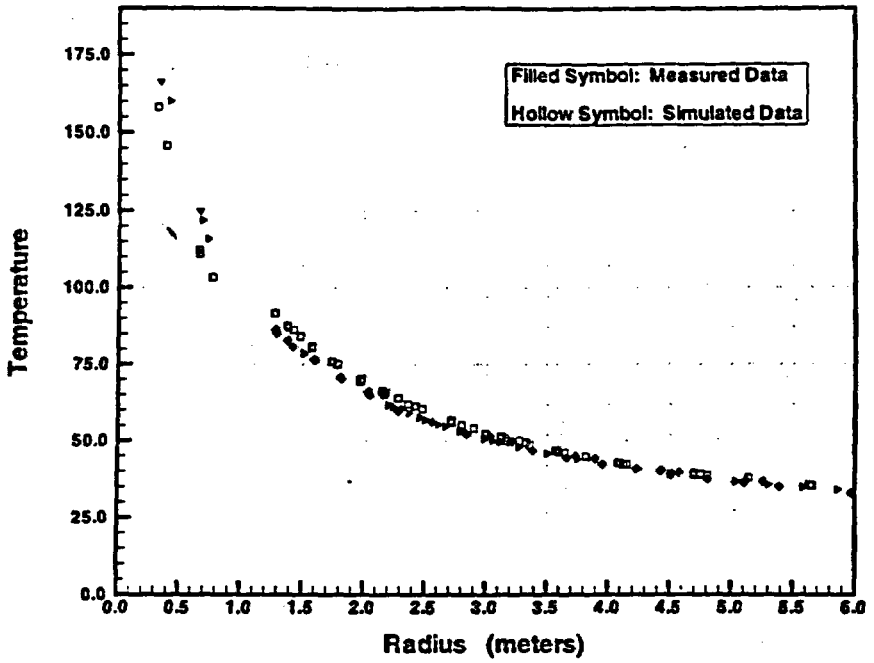

Figure 3.13 *Temperature versus radius for measured and simulated data at t = 9 months, for Case 7, at y = 4.25 m for Boreholes 2, 3, 4, 8, 9, 10, 11, 15, 16, 17,18*

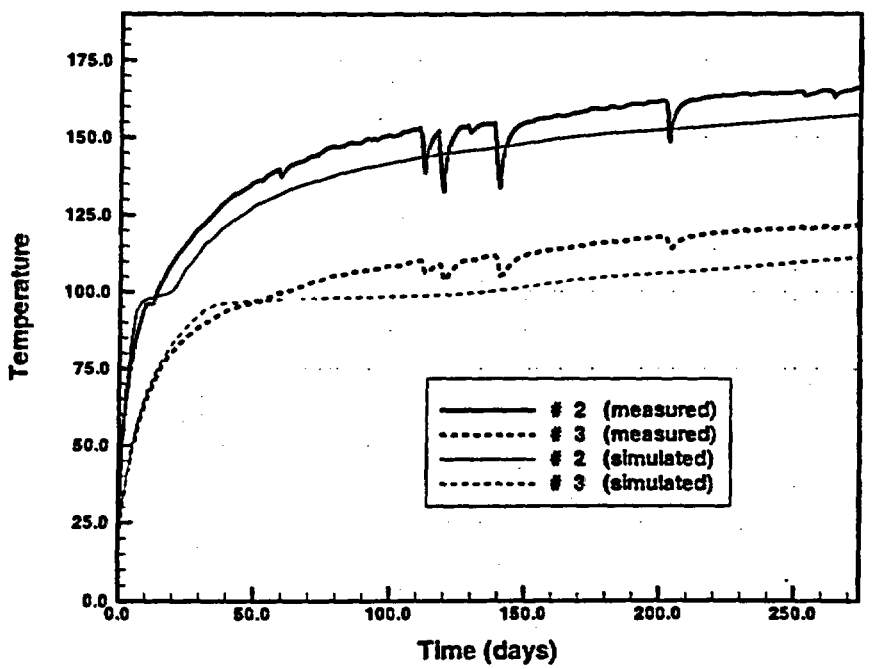

Figure 3.14 *Measured and simulated temperature evolution for Case 7, Boreholes # 2 and # 3 at y = 4.25 m*

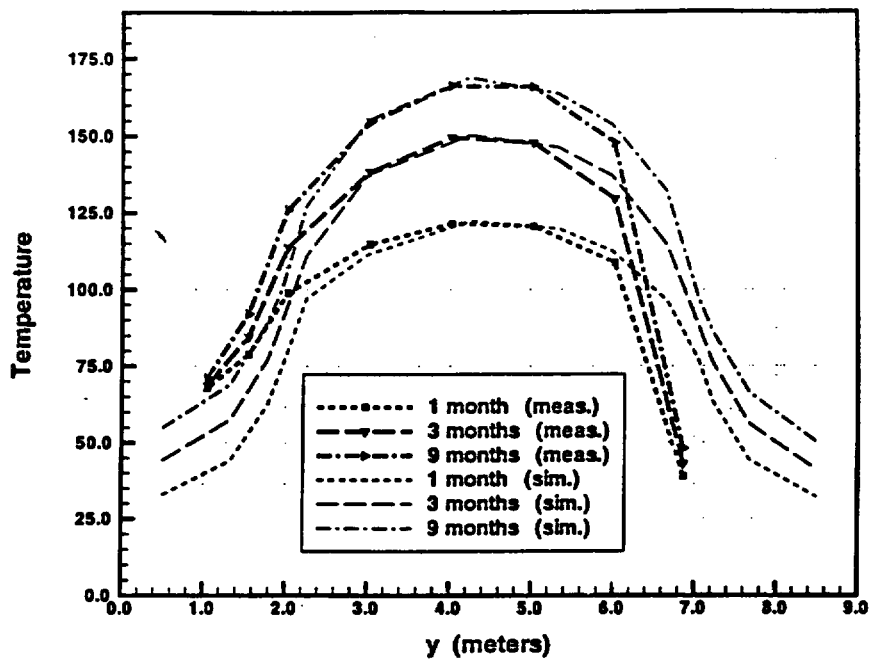

Figure 4.1 *Measured and simulated temperature profiles along Borehole # 2, for Case 4.*

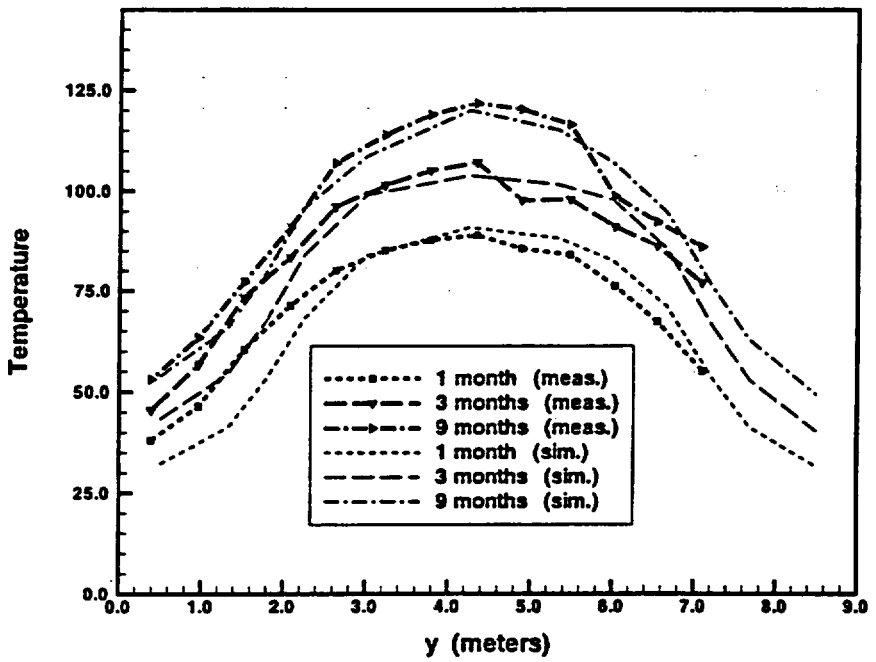

Figure 4.2 *Measured and simulated temperature profiles along Borehole # 3, for Case 4*

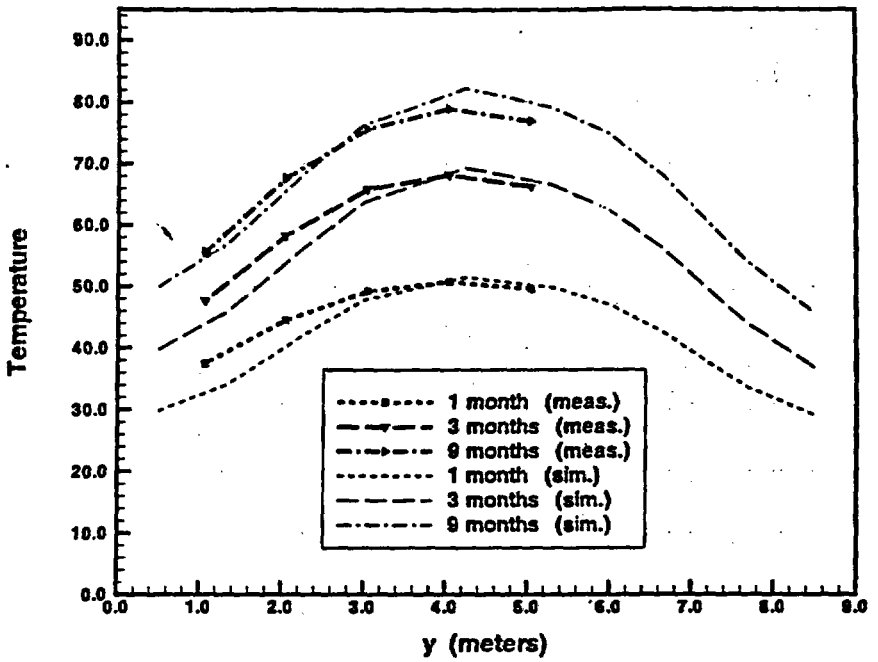

Figure 4.3 *Measured and simulated temperature profiles along Borehole # 4, for Case 4*

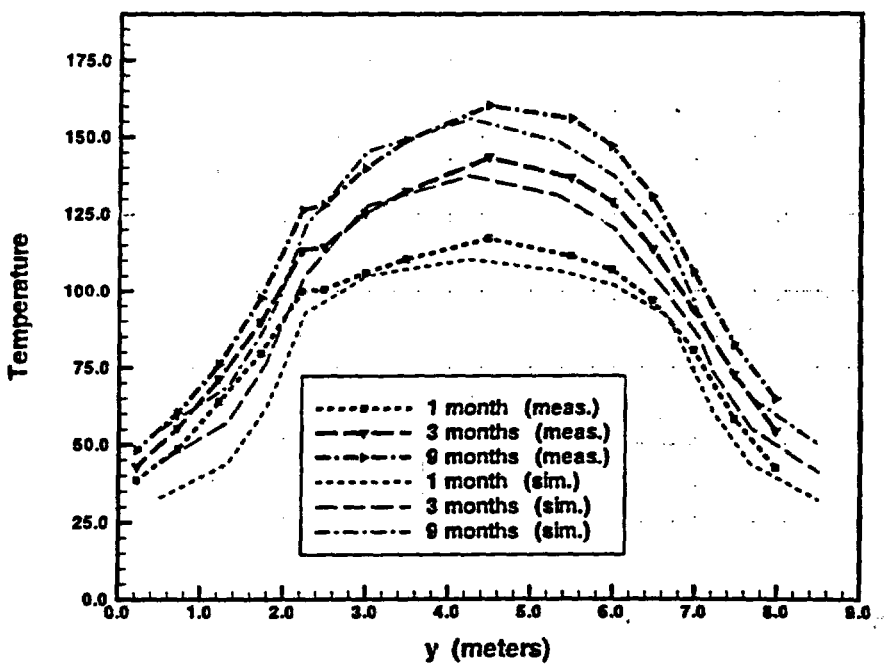

Figure 4.4 *Measured and simulated temperature profiles along Borehole # 8, for Case 4*

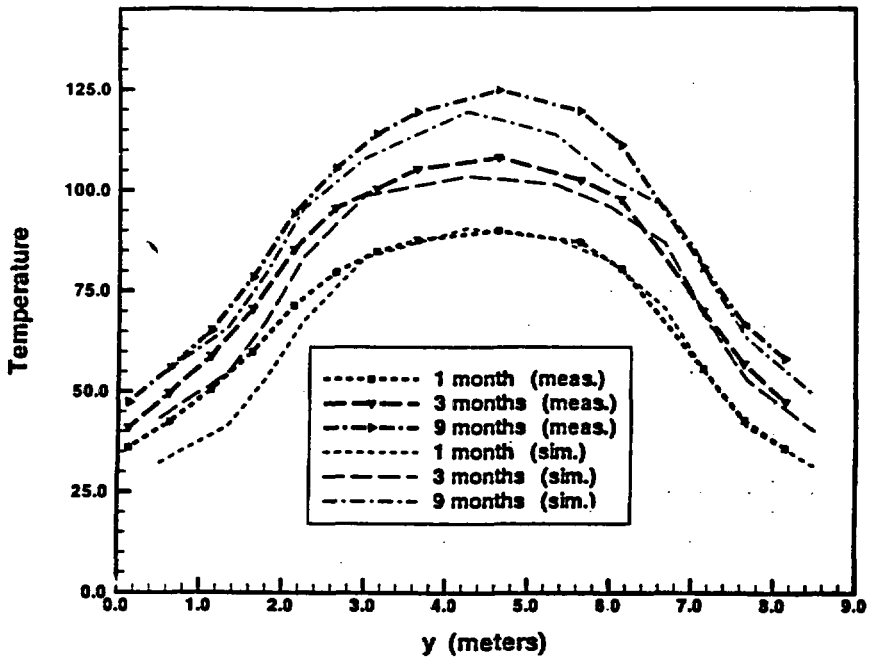

Figure 4.5 *Measured and simulated temperature profiles along Borehole # 9, for Case 4*

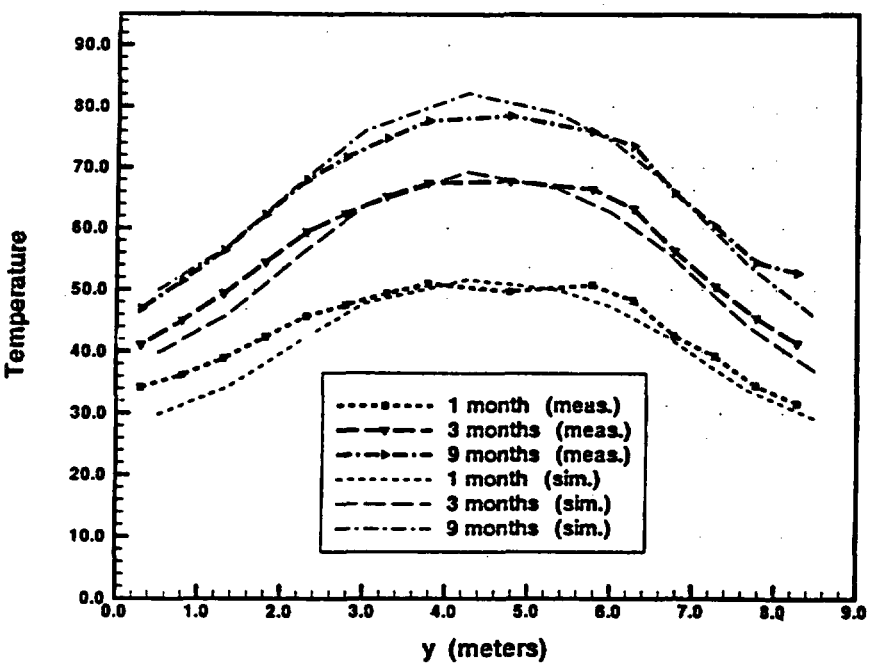

Figure 4.6 *Measured and simulated temperature profiles along Borehole # 10, for Case 4*

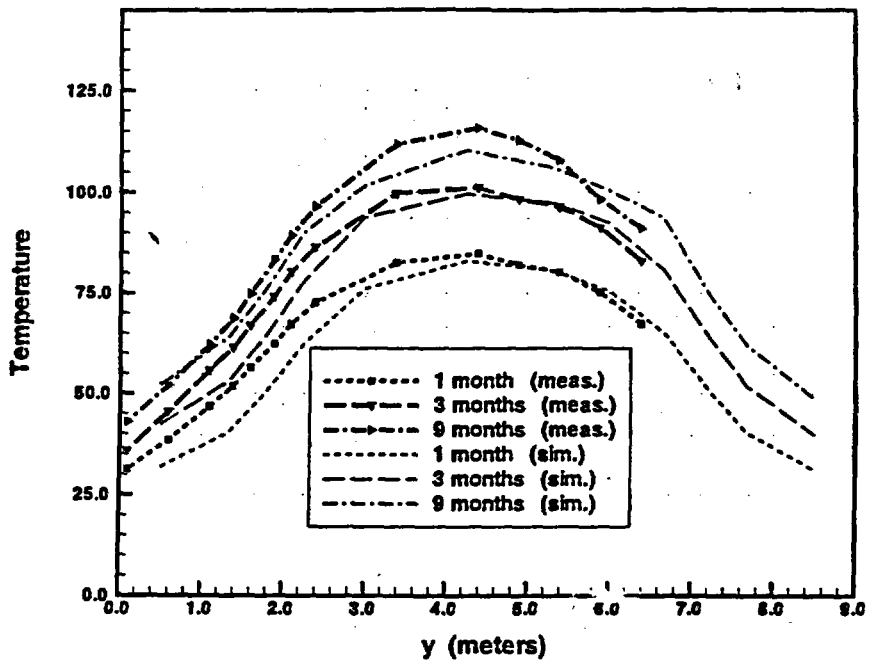

Figure 4.7 *Measured and simulated temperature profiles along Borehole # 11, for Case 4*

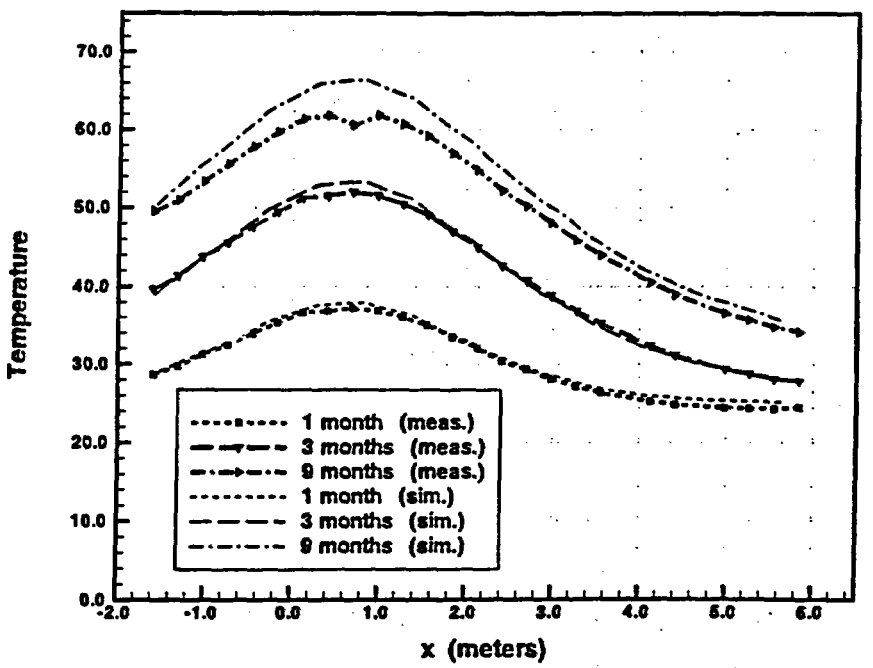

Figure 4.8 *Measured and simulated temperature profiles along Borehole # 15, for Case 4*

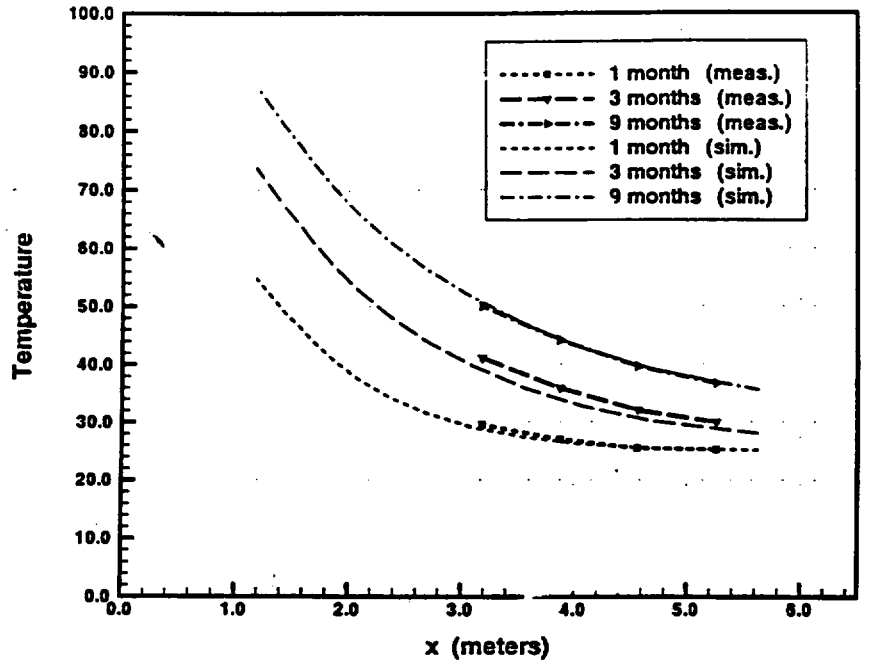

Figure 4.9 *Measured and simulated temperature profiles along Borehole # 16, for Case 4*

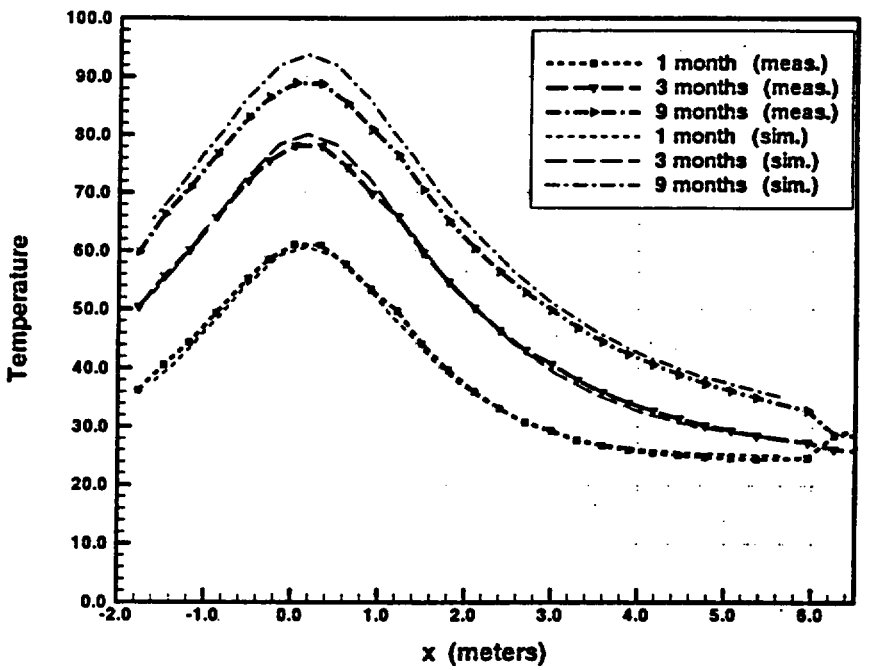

Figure 4.10 *Measured and simulated temperature profiles along Borehole # 17, for Case 4*

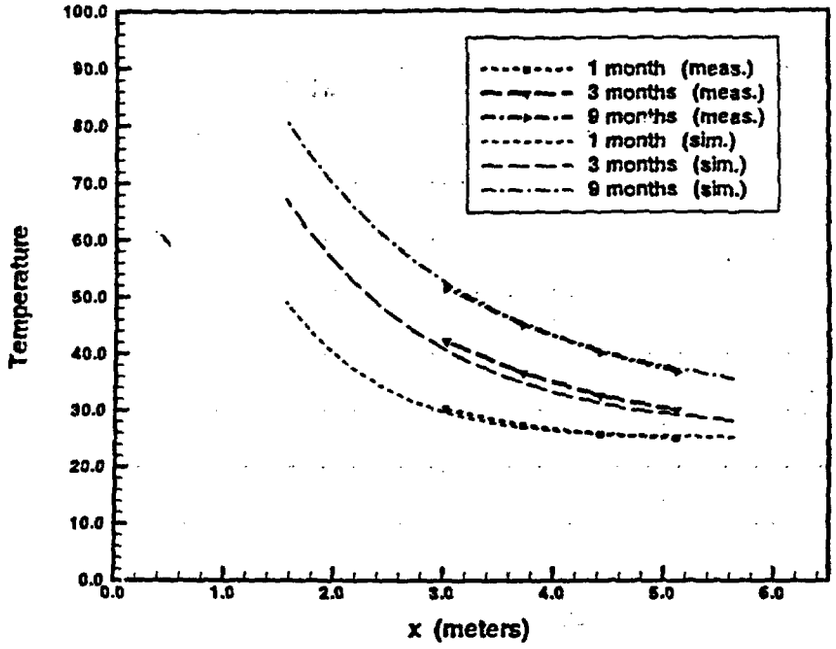

Figure 4.11 Measured and simulated temperature profiles along Borehole # 18, for case 4

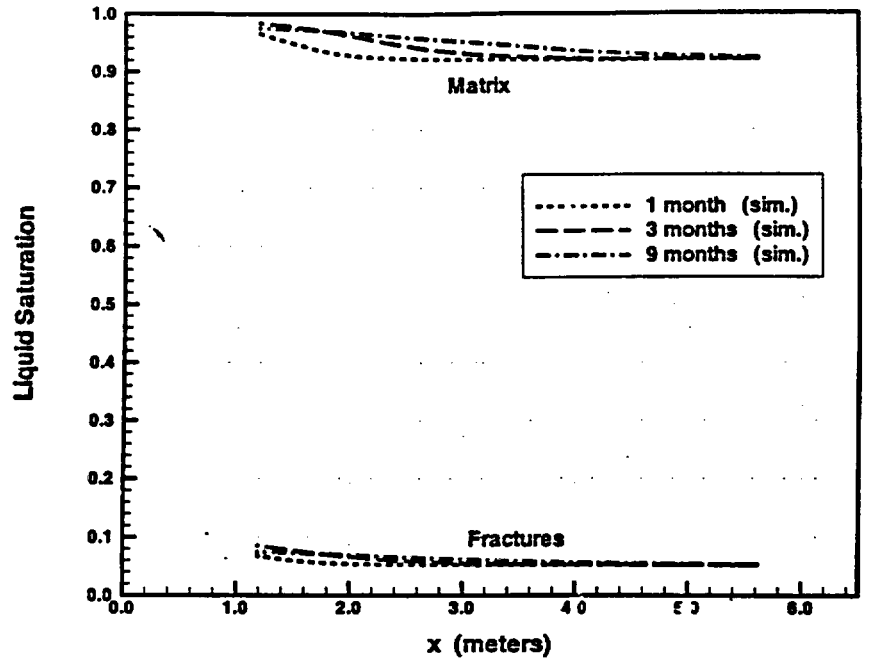

Figure 5.1 *Simulated saturation profiles along Borehole # 16, for Case 4*

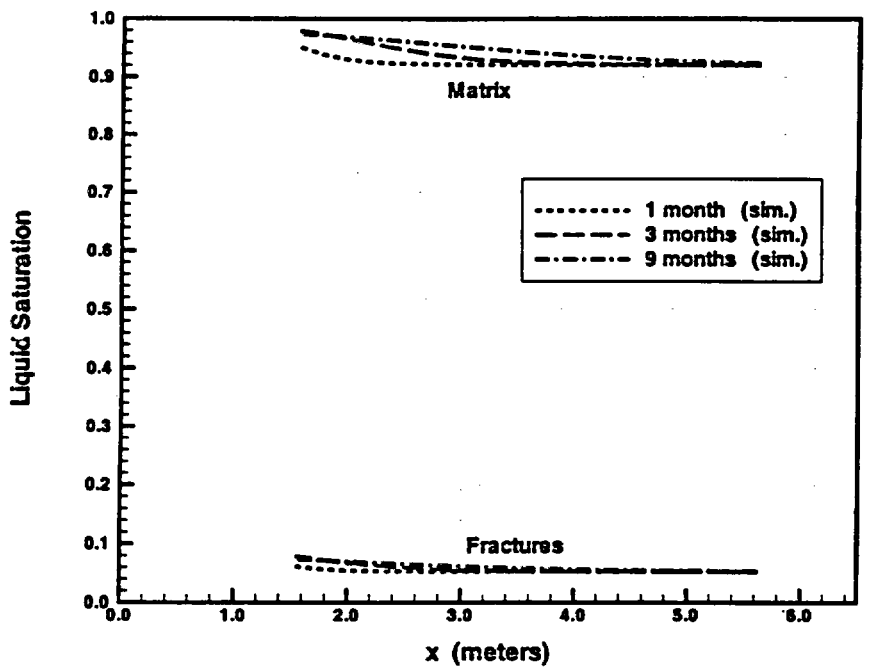

Figure 5.2 *Simulated saturation profiles along Borehole # 18, for Case 4*

DRAFT DISCLAIMER

This contractor document was prepared for the U.S. Department of Energy (DOE), but has not undergone programmatic, policy, or publication review, and is provided for information only. The document provides preliminary information that may change based on new information or analysis, and is not intended for publication or wide distribution; it is a lower level contractor document that may or may not directly contribute to a published DOE report. Although this document has undergone technical reviews at the contractor organization, it has not undergone a DOE policy review. Therefore, the views and opinions of authors expressed do not necessarily state or reflect those of the DOE. However, in the interest of the rapid transfer of information, we are providing this document for your information.